Journal of Constructional Steel Research 235 (2025) 109841

Contents lists available at ScienceDirect

Journal of Constructional Steel Research

journal homepage: www.elsevier.com/locate/jcsr

Resilient slip-friction joint (RSFJ) secondary fuse and its influence on seismic sequences☆

Nicholas Chan [a,c,*], Ashkan Hashemi [a], Pouyan Zarnani [b], Pierre Quenneville [a]

[a] Department of Civil and Environmental Engineering, University of Auckland, Auckland, New Zealand
[b] Department of Built Environment Engineering, Auckland University of Technology, New Zealand
[c] Presently at the Department of Engineering Structures, Delft University of Technology, Netherlands

ARTICLE INFO

Keywords:
Seismic
Aftershock
Damper
Self-center
Hysteresis
Degradation
Flag-shape

ABSTRACT

The Resilient Slip-Friction Joint (RSFJ) is a friction damper designed to provide stable hysteresis and self-centering behavior in its primary stage of response. Under extreme loading, a secondary 'fuse' mechanism is activated by yielding the steel rods (used as bolts), enabling additional deformation capacity. While the secondary mechanism enhances ductility, it also elongates the rods permanently, allowing the disc springs to decompress, and therefore reduce the pre-stressing forces. These can potentially degrade the joint's damping and re-centering performance in subsequent loading cycles. This study investigates whether such hysteresis degradation increases the system's vulnerability to subsequent earthquakes like aftershocks. A numerical model was developed to simulate RSFJ behavior across both primary and secondary stages, capturing key nonlinear and degradation effects consistent with experimental observations. The model was applied in a single-degree-of-freedom system to simulate a tested RSFJ-braced frame and analyzed under mainshock-aftershock sequences. Results reveal that hysteresis degradation caused the aftershock responses to amplify in proportion to the mainshock response and to the aftershock intensity ratio (AR). To mitigate the risk of bolt rupture during strong aftershocks, i.e. AR $>$ 0.8, pre-stressing losses from the initial mainshock must remain below 40–60 %. In contrast, for aftershocks with AR below 0.6–0.7, the system was generally capable of sustaining aftershocks without further deterioration regardless of the initial pre-stress loss. In sum, these findings reinforce current design practices which limit the activation of the RSFJ's secondary fuse only to strong and rare earthquakes, typically up to 1.5 times the design-level earthquake.

1. Introduction

1.1. Self-centering systems

Recent earthquakes in the 21st century have resulted in substantial socioeconomic costs on societies in terms of direct costs (e.g., structural damage) and indirect costs (e.g., protracted recovery). A well-known example is the large aftershock in Christchurch that destroyed 70 % of the city-center in 2011, one year after the initial Canterbury (Darfield) earthquake in 2010 [1,2]. Disruptive earthquakes also arise from natural and induced earthquake swarms [3,4] which, despite their relatively little damage, can cause substantial business interruption and long-term impacts on well-being [5,6].

To increase the resilience of communities against earthquake hazards [7], structures are increasingly engineered with self-centering capabilities to endure repeated earthquakes and minimize the damage and downtime after earthquakes [8]. Studies on self-centering systems have increased exponentially since 2014 in recognition of the need to reduce the disruption to society after earthquakes [9].

Various technologies have been proposed by researchers in searching for more cost-effective solutions. Examples include the use of ratcheting connectors, spring-loaded dampers, shape-memory alloys and post-tensioned steel tendons [10–12]. These devices aim to prevent or confine the damage to structures, restore structures to their original shape by eliminating undesirable residual deformations, and thus facilitate a faster recovery and return to normal operations.

☆ This article is part of a Special issue entitled: 'Connections with Fasteners' published in Journal of Constructional Steel Research.

* Corresponding author at: Department of Civil and Environmental Engineering, University of Auckland, Auckland, New Zealand.
E-mail address: jcha367@aucklanduni.ac.nz (N. Chan).

https://doi.org/10.1016/j.jcsr.2025.109841
Received 21 May 2025; Received in revised form 23 July 2025; Accepted 30 July 2025
Available online 4 August 2025

1.2. Resilient slip-friction joint (RSFJ)

This paper investigates the Resilient Slip-Friction Joint (RSFJ) as illustrated in Fig. 1. It was conceived in 2015 with the express purpose of reducing damage and downtime after earthquakes [13]. The RSFJ serves to damp earthquake-induced vibrations by dissipating seismic energy reliably via friction. Belleville springs incorporated in the joint induces both the joint and the structure to re-center during and after earthquakes. Thus, in a design scenario, the joint protects structural members from damage (as sliding begins upon exceeding a friction threshold) and it reduces the need for realignment repairs post-earthquake.

The RSFJ has been tested in various structural systems like tension-only braces, tension-compression braces, rocking timber walls and steel moment-resisting frames [14–17]. Recent shake-table tests of a three-storey steel structure has demonstrated its efficacy at self-centering and maintaining a uniform deflection profile [18]. The RSFJ's versatility has inspired further research into alternative configurations. To name a few examples, researchers have explored modifications such as using shape-memory alloys in lieu of the steel rods, swapping the disc springs for ring springs, and incorporating additional disc springs externally for multiple stages of slip [19–21].

1.3. Implications of secondary fuse

While the primary response of the RSFJ has proven to be highly repeatable in terms of a flag-shaped performance (Fig. 2), there have been limited studies on the behavior of the joint after the secondary fuse is triggered by excessive loading [22,23]. When the secondary fuse activates, the steel rods yield and elongate under tension. The elongated rod creates room for the stack of disc springs to decompress and reduce the associated clamping forces. Thus, yielding of the rod may lead to softening in the backbone curve. More importantly, the losses in pre-stressing can lead to reduced slip resistance and damping that potentially affect subsequent cycles. It is noted that Belleville washers have been used to stabilize the clamping forces for flat sliding surfaces [24]. In this case, however, pre-stressing losses remain significant because rod yielding occurs on a much larger scale of deformation that is not insignificant relative to the disc springs.

The secondary fuse response is strongly influenced by the individual components, which are characterized by nonlinear load-deformation behavior. Depending on the design of the joint, the disc springs may or may not reach the stiffening stage and the steel rods may yield with positive and/or negative stiffnesses. These components strongly influence the progressive degradation of the resulting hysteresis. How the cyclic response evolves during the secondary stage becomes a function of the components' hysteresis, the design parameters like the groove angle and the initial pre-stressing value, and finally the deformation history imposed on the joint.

The potential consequences of pre-stressing losses can be inferred from post-tensioned systems, which utilize long steel tendons to aid re-centering [25]. The loss of tension in steel tendons affect the seismic response of steel, timber and concrete frames directly [26–28]. These studies found that reduced tendon forces lead to premature activation (slip) and increased sensitivity to smaller loads, e.g., winds or minor earthquakes.

Reduced tendon forces also impair the re-centering capability. Consequently, residual deformations are reintroduced into the systems. In severe cases, the hysteresis of the system becomes pinched. The pinching is known to exacerbate displacement demands on subsequent cycles, thereby increasing the vulnerability to aftershocks [29–32]. These implications are relevant to the RSFJ because the secondary fuse can cause similar reduction in hysteretic areas.

An important difference with post-tensioned systems is that the RSFJ's friction forces are directly controlled by the pre-stressing applied on the disc springs (i.e., the clamping forces applied on the sliding surfaces). Thus, any loss of pre-stressing on the disc springs leads to a corresponding reduction in hysteretic areas and inevitably affects the damping capacity. On the other hand, systems with post-tensioned tendons tend to arrange the tendons in parallel with supplemental dampers. In such cases, the amount of dissipation is largely unaffected by the loss of tendon forces given that they function relatively independently from each other. Hence, the impact of the secondary fuse mechanism on seismic response is likely to be more significant for the RSFJ given the dependence between pre-stressing and damping forces, thus necessitating a closer examination.

1.4. Scope of the paper

Given the inherent uncertainty associated with ground motion prediction, and resulting scatter of responses from time-history analyses, there is a non-negligible possibility of exceeding the primary deformation limits of the joint. However, it is not economically feasible to prevent the activation of secondary mechanism completely by supplying a large primary deformation capacity. Indeed, in typical design scenarios the secondary fuse is intended to activate only during a maximum credible earthquake [33]. As the secondary fuse involves degrading hysteresis, it is important to understand the impact on the seismic response and the wider implications on seismic resilience, such as:

- How much is the loss of pre-stressing, and will it lower the slip force to an extent of creating serviceability issues?
- How susceptible to aftershocks after the secondary fuse has been triggered? Will it be necessary to repair or replace the device to maintain the integrity in subsequent earthquakes?

To gain insight into the above questions, this paper seeks a model that can capture both primary and secondary fuse mechanisms. A numerical model is needed to simulate the highly variable behavior, with

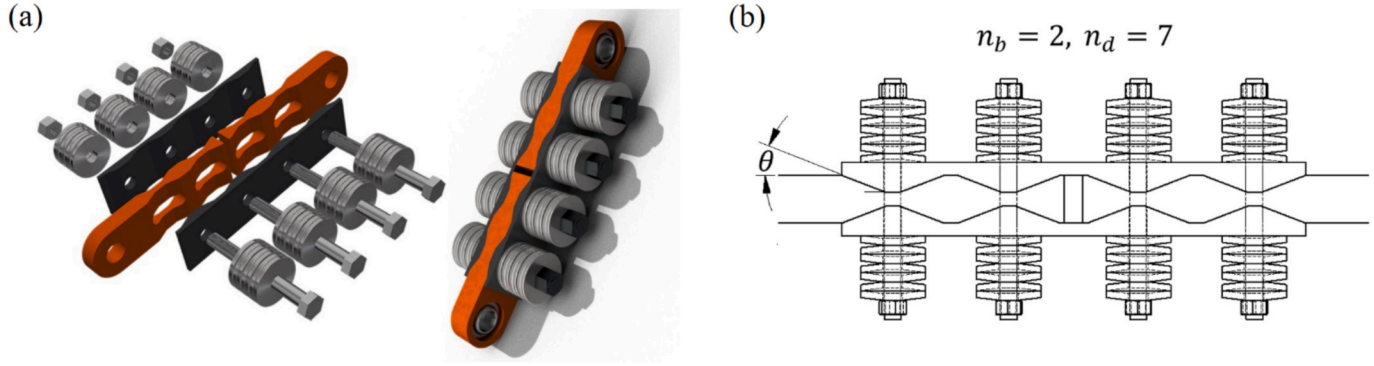

Fig. 1. Illustrating the Resilient Slip-Friction Joint (RSFJ). (a) Assembled and exploded. (b) Cross-section.

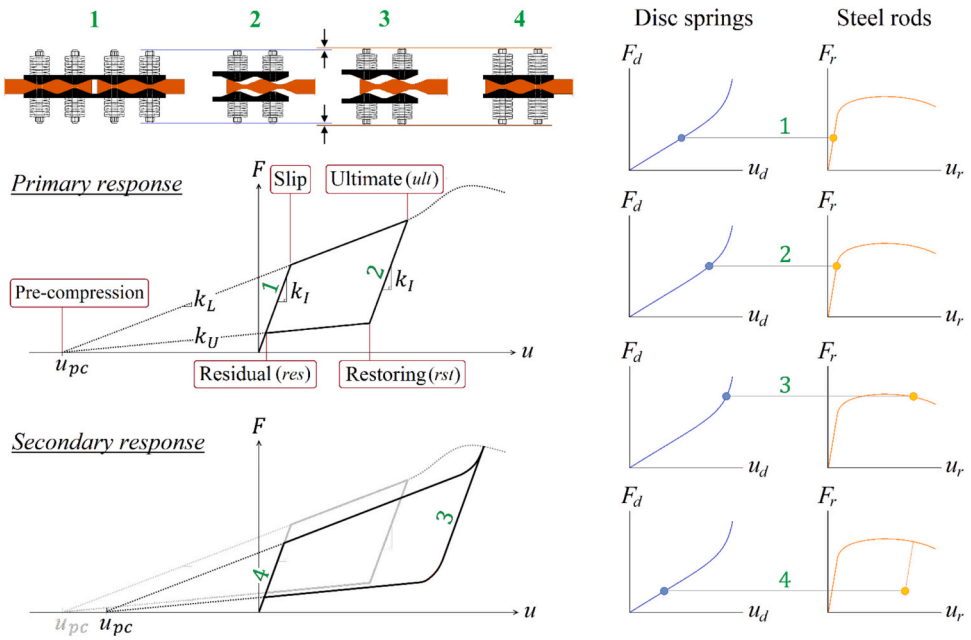

Fig. 2. Illustrating the RSFJ's primary flag-shaped response and secondary fuse response.

due consideration for the interaction between the nonlinear components (spring and rod) and their combined effect on the damper's resulting hysteresis. The model will provide the means to simulate the RSFJ's seismic response through various stages of degradation.

While the first question on serviceability issues is an important one, this paper focuses on the second question about the vulnerability to seismic sequences. For this purpose, the specific RSFJ examined in this paper represents a worst-case scenario where relatively few disc springs can lead to large pre-stressing losses. On the other hand, serviceability issues occur on a smaller scale of deformation and so are more sensitive to other factors that require consideration. These include less severe cases of pre-stressing losses; the effect of different initial stiffnesses; the level of design wind loads relative to the (dominant) earthquake loads; and the appropriate time-histories to represent wind loading. Nevertheless, by developing the tools to model pre-stressing losses, this study seeks to contribute towards future studies on serviceability aspects.

A brief description is first provided on the basic mechanics and kinematics of the damper. This is followed by a numerical method developed to calculate the hysteresis of the RSFJ through various stages of degradation. The model will be applied and compared against existing experimental data. Then, it will be used in a parametric study, which subjects a numerical model of a RSFJ-braced frame to sequences of ground motions (mainshock-aftershock). The ground motion simulations aim to shed light on the questions above and help understand the impact of the secondary fuse mechanism on the response to future/repeated earthquakes. Finally, simplified expressions are calibrated based on the parametric results to predict the subsequent behavior after the secondary fuse has been triggered.

2. Methodology

2.1. Assumed relationships

This sub-section describes the underlying mechanics and kinematics of the RSFJ assumed for the numerical model. A starting point is the established relationship between the applied forces on the joint F_a and the corresponding internal forces on the rods and discs, F_b. Basically, the axial force F_a is related to the transverse clamping forces F_b by the geometric transformation of the groove angle $\tan\theta$ and the coefficient of friction of the sliding surfaces μ. Depending on the direction of movement, the associated signs provide the resistance encountered while the joint is sliding. This is the top branch when the joint is opening or loading (e.g., slip to ultimate), or the bottom branch when the joint is closing or unloading (e.g., restoring to residual). The term $2n_b$ in Eq. (1) accounts for the total number of rods (bolts).

$$F_a = 2n_b F_b \frac{\tan\theta \pm \mu}{1 \mp \mu\tan\theta} \tag{1}$$

Eq. (2) shows, in incremental form, the relationship between the external/applied deformation on the RSFJ assembly u_a, and the deformation of the internal components. The internal components comprise the steel rod u_r, the disc springs u_d, and the elastic deformation of the steel (grooved) plates u_e that give rise to the slope k_I in Fig. 2.

$$\Delta u_a = \frac{\Delta u_r + \Delta u_d}{\tan\theta} + \Delta u_e \tag{2}$$

Sliding begins when the friction is exceeded during the calculation of a trial step. Under loading, the joint may continue to open wider only if the trial axial force rises above a factor pp of the transverse force, whereby $p = (\tan\theta + \mu)/(1 - \mu\tan\theta)$. Conversely, the joint may continue to close during unloading only if the trial axial force falls below a factor nn of the total transverse force, whereby $n = (\tan\theta - \mu)/(1 + \mu\tan\theta)$. Between these limits, the step change in force is therefore simply $k_i \Delta u_a$ which comprise of elastic deformation only ($\Delta u_a = \Delta u_e$) seeing as the other rod and disc deformation components are unchanged until friction is overcome.

2.2. Rupture deformation

In theory, the rod could rupture earlier than expected and prevent the rod's deformation capacity from being fully utilized or translated into joint axial deformation. As the rod loses strength post-peak, it may arrive at a critical tipping point whereby the disc springs continue to decompress and push the rod to rupture, despite no increment in axial deformation applied to the joint. The instability and uncontrolled decompression could initiate at the point when the absolute stiffness of the rod becomes steeper than the disc springs.

The events leading to rupture in Fig. 3 can be described as follows. On the verge of instability at point *a*, rod and disc forces are in equilibrium with the same tangent stiffnesses. Beyond this point however,

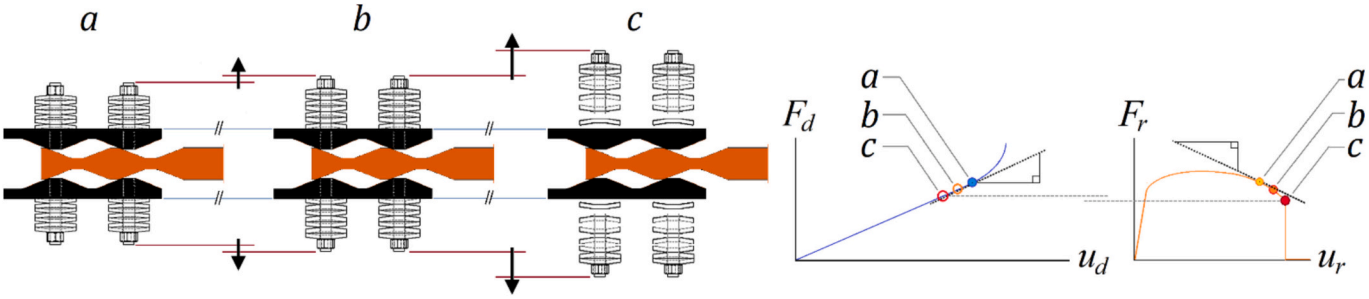

Fig. 3. Potential point of instability (uncontrolled decompression) assumed in the absence of a tertiary fuse.

disc forces become greater than rod forces at points *b* and *c* for the same change in deformation. The unbalanced forces cause the rod to continue yielding until it ruptures. There is no recovery from this because the stiffness of the rod will continue to be steeper than the stiffness of the discs, such that rod forces will always decrease more than disc forces and exacerbate the force imbalance or instability. Hence, the maximum deformation of the RSFJ is effectively limited to the axial deformation corresponding to point *a*.

This is more likely to occur with (1) tall stacks of disc springs resulting in low spring stiffness, which implies a large reservoir of potential energy beyond what is available from the rods plasticity, (2) steel rods that lose strength gradually, such that the post-peak stiffness decreases over a large deformation, and therefore increase the likelihood of stiffness crossover long before the rod's fracture deformation. In any case, a conservative assumption for the numerical model is to take the critical deformation at the stiffness crossover as the limiting (rupture) deformation of the joint.

One aspect that has not been considered in this study is that the RSFJ may possess additional capacity to resist further loads and avoid a catastrophic rupture. This is possible if the rods are designed to reach the end of the slotted holes within the middle plates (colored orange in Fig. 3). When this occurs, the rods are subjected to additional shearing forces at the shear planes between the (orange) middle plates and (black) outer plates.

While the potential increase in ductility is currently unknown, the additional shear capacity implies increased force resistance from the joint. When this happens, the joint is no longer the weak link and thereby causes a redistribution of forces to other parts of the structure. Hence, designers will necessarily consider other fuses in the hierarchy of ductility. For the purposes of this study, the additional shearing capacity is conservatively ignored given the uncertainties surrounding the possible increase in ductility or brittleness from other parts of the system.

2.3. Numerical procedure

This section outlines the steps of the numerical procedure. It is essentially an incremental procedure that takes the current state parameters as inputs. It attempts to seek and output the necessary increments in deformations within the rods and discs, which altogether result in the required step change in RSFJ axial deformation. At the same time, the increment in rod and disc forces must also maintain force equilibrium. To begin, the following inputs are specified and converted into more convenient forms for calculation:

- Specify RSFJ properties k_I, F_{ps}, μ, θ, n_b and calculate the sliding threshold p, n (Section 2.1).
- Specify backbone curves for the rods and discs. Transform backbone curves into equivalent curves by scaling according to the number of rods and disc stacks.
- Pre-calculate the deformations of the rod, disc, and joint at the instance of rupture.

Having established the properties of the joint and internal components, the procedure must now determine the current state of the joint before calculating the state at the next increment. The checks required are:

- Check whether the rod has ruptured, and if not, then calculate how much yielding has occurred.
- Determine whether the joint is opening, closing, or responding elastically in the next (sub-)step. This is determined by checking whether the friction resistance will be exceeded.
- In the case of the joint sliding close, the tangent stiffness of the joint is used to check for the transition from sliding (closing) to elastic (closed). This simplifies the check and reduces the possibility of cumulative errors from using the disc and rod deformation.

Having determined the current state, the procedure now calculates the state at the next step. The task is to seek the corresponding increments in rod, disc and plate deformations that sum altogether to the required increment in RSFJ axial deformation, after applying the necessary transformation as per Eq. (2). At the same time, the forces obtained in the rod and the disc must be equal, since they are arranged in series with each other. Given these constraints, the iterative solution method can be described as follows:

1) Iterate for the rod, disc and plate deformation. Use 1(a) if the joint is sliding open (loading) to easily handle rod rupture and yield plateaus. Use 1(b) if the joint is sliding close (unloading) to easily quantify the slack in disc springs when the forces are zero.
   a. Calculate upper and lower bounds for the increment in rod deformation. Select a value (e.g., bisection method selects the midpoint) and calculate the corresponding increment in rod force. Using the same force increment for the disc, calculate the corresponding increment in disc deformation.
   b. Calculate upper and lower bounds for the increment in disc deformation. Select a value (e.g., bisection method selects the midpoint) and calculate the corresponding increment in disc force. Using the same force increment for the rod, calculate the corresponding increment in rod deformation.
2) Calculate the resulting axial deformation. Transform these deformation components to the axial direction and sum with the elastic plates' deformation increment to obtain the total axial deformation.
3) Convergence check. If the resulting axial deformation deviates from the required axial deformation beyond the specified tolerance, return to the first step and repeat the iterations.
4) Update the state variables and proceed to the next (sub-)step, starting with state determination and then repeating the iterations above.

The required increment/step in RSFJ axial deformation may also be broken down into sub-steps if transitions are detected between the current step and the next step. By doing so, the hysteresis calculations will have greater accuracy even if multiple transitions occur within a single step. Some examples of stiffness transitions are:

- Transition when sliding starts or stops due to friction,
- Transition of the rod between elastic and plastic states, and plastic to rupture
- Transition of the disc between slackness (fully decompressed) and loaded states

One benefit of decomposing the step into sub-steps is easier convergence on the required deformation increment. From observation, a generous tolerance of 0.1–0.2 times the step size can provide satisfactory results in pushover analyses, when used in conjunction with a tighter tolerance specifically for transitions, i.e., 2(eps) or 2(eps) times the sub-step size, whichever is larger. In time-history analyses, the tolerance of machine epsilon (eps) is needed to maintain accuracy since the deformation increments are generally much smaller, especially with small timesteps. For simplicity, the bisection method is implemented to iterate and converge on the step change required.

3. Parametric study

3.1. SDOF model of the braced frame

A parametric study was conducted to understand how the secondary fuse can impact the resilience of the system against future earthquakes like aftershocks. For this purpose, a series of incremental dynamic analyses were performed to obtain a range of deterioration states (i.e., different losses in pre-stressing). This is illustrated in Fig. 4. Subsequently, each state was subjected to various levels of aftershocks to determine any changes in behavior during the aftershock following the initial mainshock. Section 3.3 describes the excitations in more detail.

The single-storey steel frame was tested by Bagheri et al. [22] using RSFJ in tension-only braces. The size of the frame was 5.05 m wide by 3.1 m tall. RSFJs were bolted to the diagonal braces, which were M24 steel rods (Grade 8.8). They were tightened by hand until the slender rods were no longer sagging. While tightening the cross-braces puts the frame in a state of stress, this stiffening only affected the upright position (zero displacement) because the diagonal braces were not loaded simultaneously when swaying. A string potentiometer was used to measure the lateral displacements of the frame. It was attached to a datum pole at one end, and to the steel frame at the other end at approximately the same height as the actuator. Load measurements were obtained from the actuator's load cell.

Fig. 4(a) shows the cyclic behavior of the frame. A displacement of 75 mm (at approx. 2.5 % drift) delineates the primary and secondary stages of response, above which the pre-stressing losses begin to accrue. The intention was to activate the secondary mechanism upon exceeding the ultimate limit state (ULS) design earthquake intensity. The displacement capacity of the frame also satisfies the minimum requirement of MCE earthquakes, which is 1.5 times the ULS displacement of 75 mm or approximately 113 mm.

To simplify the modelling, the numerical model intended for the RSFJ was calibrated to represent the single-storey frame as a single degree-of-freedom (SDOF) system. The numerical model from Test 3 (Section 4.1) was modified for this purpose, using additional scale factors of 2/0.85 for the rod and disc deformations. This is because two

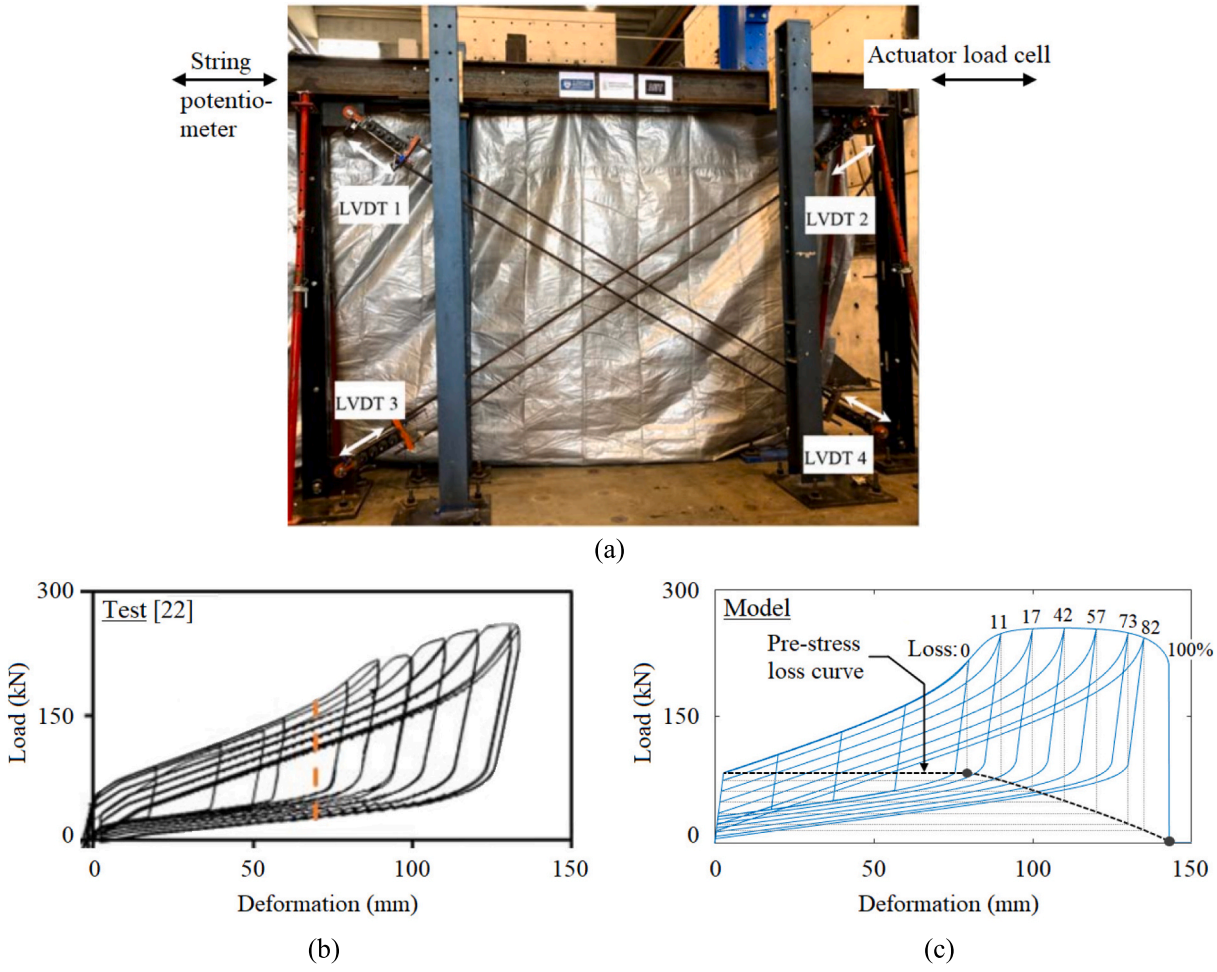

Fig. 4. Modelling the single-storey braced frame tested by Bagheri et al. [22]. (a) Test set-up. (b) Test data. (c) Hysteresis simulated using the proposed numerical model.

joints were arranged in series within the brace. Furthermore, the axial (diagonal) deformation of the braces was translated to a horizontal displacement at $\cos(32^{\circ}) = 0.85$ times the diagonal deformation in the braces. Hence, the forces in the RSFJ (via the rod and disc backbones) were also multiplied by 0.85 to translate the axial forces into horizontal forces acting on the frame.

Finally, k_i and F_{ps} were adjusted to 30 kN/mm and 45 kN respectively to produce the curves in Fig. 4(b). The pre-stress loss curve indicates the percentage loss of pre-stress corresponding to the deformation sustained. In other words, it shows how the slip forces reduce with increasing peak deformation. This is also shown in Table 1 for a select number of points.

As for the SDOF dynamic properties, the fundamental period was estimated from clause C4.1.2 of the New Zealand standard NZS 1170.5 [34]. It is $T_1 = 1.25k_th^{0.75} = 0.219$ s, with k_t being 0.075 for steel braced frames, and the height h being 3.1 m tall. The initial stiffness from the test result in Fig. 4 is approximately k = 30 kN/mm. Therefore, the mass assigned to the SDOF is $m = k/w^2 = 36{,}500$ kg. A damping ratio of 1 % was assigned to the SDOF model based on test data [18].

3.2. Time-stepping procedure

Nonlinear time-history analyses were conducted to examine the seismic response of the steel braced frame. The time-stepping method used was Newmark's beta method with linear acceleration ($\gamma = 1/2$, $\beta = 1/6$) for greater accuracy. The algorithm has been used in a previous parametric study performed for flag-shaped hysteresis and validated with other structural analysis programs as far as the primary response is concerned [35]. The timesteps used were 0.002 s, which is finer than the timestep required for conditional (numerical) stability of 0.12 s as Eq. (3) shows. Timesteps of the ground motions were also refined by linear interpolation to match the analysis timestep.

$$\Delta t > \frac{T}{\pi\sqrt{2(\gamma - 2\beta)}} = 0.12 \text{ sec} \tag{3}$$

The Newton-Raphson method was used to solve for the state variables (u, v, a, f_s, k_t) and satisfy dynamic equilibrium at each timestep [36]. These variables are displacement, velocity, acceleration, hysteretic force and tangent stiffness. Each iteration of the Newton-Raphson method utilized the iterative procedure described in Section 2.3 for calculating the RSFJ hysteresis over the deformation increments.

The tolerance used to converge on the deformation increment at each iteration was specified at 2(eps). When the velocity sign changes, the reversal of direction was handled by seeking the instance of reversal and thus splitting the timestep into two sub-steps [37]. The Brent-Dekker method was used to identify the point of reversal to a tolerance of one-hundredth of the timestep [38].

3.3. Ground motions

A set of 52 ground motions were selected from the PEER NGA-West2 database [39]. They were selected based on the goodness-of-fit to a design spectrum used for Wellington, New Zealand [34]. The parameters chosen for the ultimate limit state (ULS) design spectrum was soil class D, located within 20 km to the nearest fault, and a return period of 500 years. The fit was assessed over a period range of 0.1 to 2 s. An additional criterion was imposed to filter the ground motions by limiting the scale factor to below 10. This led to the 52 ground motions listed in Table 2 and the scale factors k_{ULS} used to scale their spectra to the design spectrum. Fig. 5(a) shows the amplitude-scaled spectra for this set of ground motions.

In addition to the set of amplitude-scaled ground motions in Fig. 5 (a), another set of 52 ground motions was also prepared using the spectral matching procedure to reduce the variance and increase the precision of the responses obtained [40]. The acceleration spectra for the spectral-matched ground motions are shown in Fig. 5(b). The spectral-matched ground motions were derived from the amplitude-scaled ground motions, by using them as seed motions to minimize the amount of modification needed.

The spectral matching procedure involves solving a set of simultaneous equations for the n wavelets needed to correct the mismatch between the ground motion's spectrum and the target spectrum at n period points [41]. Each iteration involves recomputing the responses to the modified ground motion and the new corrections (wavelets) required. The iterations were performed until the error from the target spectrum was within 1 % (on average) and 5 % (maximum deviation) across n = 100 period points, but not more than 30 iterations. Several combinations of pre-stressing loss and mainshock-aftershock sequences were investigated as shown in Table 3.

Fig. 6 describes the steps involved in a typical analysis. It uses an example with 20 % loss in pre-stress resulting from a mainshock (RSN1013 – LA Dam), and a selected aftershock (RSN1063 – Rinaldi) scaled by AR = 1.0 which resembles a very strong aftershock. In this case, the steps involved would be:

- First, the mainshock (LA Dam) is applied after it has been scaled by $k_{MAIN} = k_{ULS}{*}k_{Target} = 1.41{*}1.25 = 1.763$ with these scale factors being specific to RSN1013 (refer to Tables 2 and A1). These factors cause a 20 % loss of pre-stress to the *virgin* system (i.e., no prior yielding / secondary fuse). In this study, the scale factors were found via the bisection method with convergence tolerance of 0.01 mm within the target displacements.
- The mainshock is followed by a 30 s interval to damp the vibrations, with a damping ratio of 1 % and vibration period of 0.22 s. According to Pirooz et al. [42], this time gap between mainshock and aftershock is sufficient to reduce the velocity to about 1/1000 of the peak value.
- Then, the aftershock (Rinaldi) is applied after it has been scaled by $k_{AFTER} = AR{*}(k_{ULS}{*}k_{Target}) = 1.0{*}0.86{*}1.39 = 1.195$ as these factors are specific to RSN1063 (refer again to Tables 2 and A1).
- Record the peak responses after the mainshock and the aftershock.
- Repeat the analyses for the next combination of pre-stress loss (target disp.) and aftershock intensity.

4. Results and discussion

4.1. Comparison with experimental data

A previous study by Bagheri et al. [22] tested the RSFJ for an application in a steel braced frame. Fig. 7 shows the joint which was loaded until the rods ruptured. Figs. 7(b) and 7(c) show the representative backbone curve for the stack of five discs and for the steel rod. These are representative curves because the authors noted some variation in test data, especially for the steel rods' strength and deformation capacities. Because of the variation, each of the three tests produced different hysteresis with different pre-stressing losses and rupture deformations as Figs. 7(d)–7(f) show.

Table 1
Selection of 15 target displacements and the corresponding pre-stress losses used in the analyses.

Point	1	2	3	4	5	6	7	8	9	10	11	12	13	14	15
U_{max} (mm)	15	30	45	60	76	89	96	103	109	115	122	128	134	139	143
F_{slip} (kN)	84	84	84	84	84	75	67	59	50	42	33	25	17	8	0
PS Loss (%)	0	0	0	0	0	10	20	30	40	50	60	70	80	90	100

Table 2
Ground motions used to create the mainshock-aftershock sequences.

RSN	Earthquake Event	Station Name	Year	M_w	k_{ULS}
6	Imperial Valley-02	El Centro Array #9	1940	6.95	2.12
135	Santa Barbara	Cachuma Dam Toe	1978	5.92	9.26
138	Tabas_ Iran	Boshrooyeh	1978	7.35	4.30
161	Imperial Valley-06	Brawley Airport	1979	6.53	2.29
215	Livermore-01	San Ramon Fire Station	1980	5.8	9.45
266	Victoria_ Mexico	Chihuahua	1980	6.33	2.55
268	Victoria_ Mexico	SAHOP Casa Flores	1980	6.33	6.60
316	Westmorland	Parachute Test Site	1981	5.9	2.34
358	Coalinga-01	Parkfield - Stone Corral 4E	1983	6.36	6.58
366	Coalinga-01	Parkfield - Vineyard Cany 6 W	1983	6.36	8.61
502	Mt. Lewis	Halls Valley	1986	5.6	3.09
504	Taiwan SMART1(40)	SMART1 E01	1986	6.32	3.15
523	N. Palm Springs	Indio - Coachella Canal	1986	6.06	9.33
569	San Salvador	National Geografical Inst	1986	5.8	1.14
721	Superstition Hills-02	El Centro Imp. Co. Cent	1987	6.54	1.61
729	Superstition Hills-02	Imperial Valley Wildlife Liquefaction Array	1987	6.54	1.51
798	Loma Prieta	SF - Telegraph Hill	1989	6.93	8.95
802	Loma Prieta	Saratoga - Aloha Ave	1989	6.93	1.32
821	Erzican_ Turkey	Erzincan	1992	6.69	1.10
827	Cape Mendocino	Fortuna - Fortuna Blvd	1992	7.01	3.57
832	Landers	Amboy	1992	7.28	3.87
930	Big Bear-01	San Bernardino - 2nd & Arrowhead	1992	6.46	4.76
1013	Northridge-01	LA Dam	1994	6.69	1.41
1063	Northridge-01	Rinaldi Receiving Sta	1994	6.69	0.86
1119	Kobe_ Japan	Takarazuka (NS)	1995	6.9	0.71
1119	Kobe_ Japan	Takarazuka (EW)	1995	6.9	0.71
1137	Dinar_ Turkey	Burdur	1995	6.4	9.93
1148	Kocaeli_ Turkey	Arcelik	1999	7.51	4.53
1165	Kocaeli_ Turkey	Izmit	1999	7.51	2.52
1268	Chi-Chi_ Taiwan	HWA017	1999	7.62	5.27
1773	Hector Mine	Cabazon	1999	7.13	9.99
1823	Hector Mine	Salton City	1999	7.13	8.01
2115	Denali_ Alaska	TAPS Pump Station #11	2002	7.9	8.87
2958	Chi-Chi_ Taiwan-05	CHY054	1999	6.2	8.39
3577	Taiwan SMART1(5)	SMART1 O10	1981	5.9	5.86
3746	Cape Mendocino	Centerville Beach_ Naval Fac	1992	7.01	1.21
3754	Landers	Indio - Jackson Road	1992	7.28	3.11
4113	Parkfield-02_ CA	Parkfield - Fault Zone 9	2004	6	4.54
4117	Parkfield-02_ CA	Parkfield - Fault Zone 15	2004	6	2.92
4366	Umbria Marche (aftershock 1) Italy	Gubbio-Piana	1997	5.5	8.66
4457	Montenegro_ Yugoslavia	Ulcinj - Hotel Albatros	1979	7.1	1.92
4483	L'Aquila_ Italy	L'Aquila - Parking	2009	6.3	1.62
4840	Chuetsu-oki_ Japan	Joetsu Kita	2007	6.8	2.60
4855	Chuetsu-oki_ Japan	Sanjo	2007	6.8	3.46
5470	Iwate_ Japan	AKT015	2008	6.9	8.12
5779	Iwate_ Japan	Sanbongi Osaki City	2008	6.9	3.71
5831	El Mayor-Cucapah_ Mexico	EJIDO SALTILLO	2010	7.2	2.69
6014	El Mayor-Cucapah_ Mexico	Mecca Fire Station	2010	7.2	7.87
6890	Darfield_ New Zealand	Christchurch Cashmere High School	2010	7	1.75
6988	Darfield_ New Zealand	WSFC	2010	7	6.57
8130	Christchurch_ New Zealand	Shirley Library	2011	6.2	1.14
8134	Christchurch_ New Zealand	Styx Mill Transfer Station	2011	6.2	3.01

Table 4 shows the inputs for the numerical model. Given that the variation in steel rods affected the test results significantly, a limited amount of variation was also allowed in the inputs for the model. Scale factors were applied to the rod backbone – $SF(\Delta_{rod})$ and $SF(F_{rod})$ – based on the range observed by Bagheri et al. [22]. The pre-stressing F_{ps} was also adjusted to reflect the differences in the slip forces. This variation is due to the manual process of pre-stressing the disc springs by hand, with a maximum deviation of about 10 % allowed from the targeted slip force.

The results show that the numerical procedure can predict the response of the RSFJ sufficiently from primary to secondary stages of response. The pre-stressing losses over multiple cycles can be replicated as shown in Figs. 7(g)–7(i). The rupture deformations from the numerical modelling also varied similarly with the test results. However, a slight difference in Figs. 7(f) and 7(i) can be seen, as the former continued to harden towards the peak load, while the latter reaches a load plateau as per the backbone curve assumed for modelling the steel rods.

4.2. Response to design (ULS) ground motions

The following results pertain to the time-history analyses conducted on the simulated braced frame (Section 3.1). For ground motions scaled to the design (ULS) intensity, the displacement response is estimated to range between 60 and 63 mm (approximately 2 % drift) depending on the set of ground motions used. Comparing the two sets of ground motions, the average displacements differed by 2.4 % only and the median displacements by 3.4 %. The standard deviation and median absolute deviation (M.A.D.) were smaller for the spectral matched records as shown by the distribution of responses in Fig. 8. On average, the displacement response satisfies the design intent as it falls within the primary phase with undegraded flag-shaped behavior and without any pre-stressing losses.

The maximum displacement across all records was 96 mm (10 % loss) and 104 mm (20 % loss) for the amplitude-scaled and spectral-matched records respectively. As a set however, the pre-stressing losses are minor since the 95th percentile displacement was only 93 mm and 82 mm respectively. The small pre-stressing losses indicate that the system was designed appropriately to respond to the design (ULS) ground motions within the primary stage and without degradation of its flag-shaped behavior.

Looking at the scale factors k_{Target} in Appendix A, it is found that the MCE scale factor is approximately 1.5 times the ULS scale factor if it is assumed that the MCE displacement corresponds to 60–70 % pre-stressing loss. The ULS displacement is taken as the scale factor corresponding to 60 mm according to the response to ULS ground motions in Fig. 8. The ratio of 1.5 matches the design guidelines [34]. Thus, the secondary fuse is appropriately designed for its purpose of resisting stronger and rarer ground motions at the MCE intensity.

4.3. Response to a ground motion sequence

The ground motions were scaled further giving a final scale factor of $k_{ULS}k_{Target}$ to achieve the specified deformations and pre-stressing losses. The iterative bisection method was used to find the scale factors required for each ground motion; these scale factors are listed in Appendix A. Table 5 shows that the scale factors obtained were sufficiently accurate at a select number of points. On average, the error in displacements across all ground motions ranges between 0.00 and 0.08 % for the set of amplitude-scaled records, and 0.00–0.23 % for the set of spectral-matched records.

Fig. 9 shows an example of the responses to the scaled ground motions. For illustration purposes, two ground motions from Table 3 are used here with RSN1013 as the mainshock and RSN1063 as the aftershock. From left to right, the pre-stressing losses after the mainshock are 0 %, 20 % and 40 % as shown by the blue dashed lines (RSN1013). At 0 % loss of pre-stressing, the response to the mainshock occurs entirely in the primary stage while the responses from 20 % and 40 % losses reach into the secondary stage.

From top to bottom, the aftershock ratios are 1.0 and 0.75. With an aftershock ratio of 1, the aftershocks are scaled to reach the same

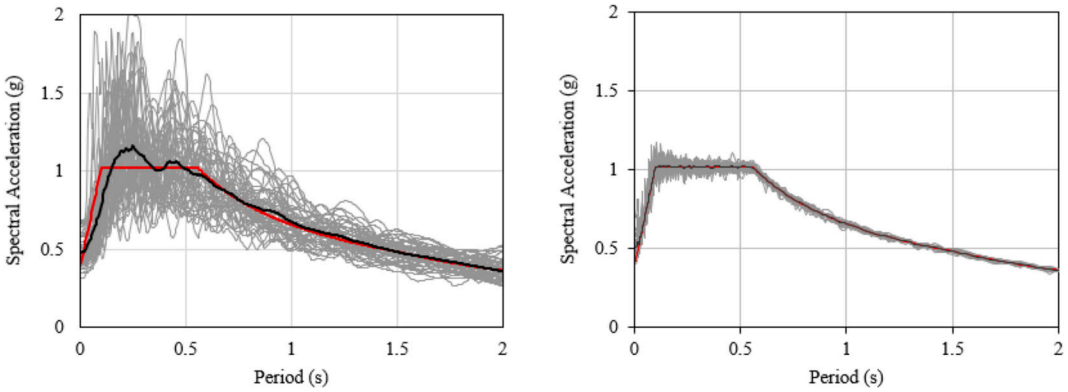

Fig. 5. Ground motion acceleration spectra after (a) amplitude-scaling, and (b) additional spectral matching.

Table 3
Range of parameters examined in the study.

Varied Parameters	Range/Type of Variations
Ground motion selection	– All possible combinations of 52^2 mainshock-aftershock pairs from the set.
Ground motion scaling to the design spectrum	– Set 1 (amplitude-scaling): scale by k_{ULS}, then scale by $k_{Target\ (1)}$ to achieve the required pre-stressing loss. – Set 2 (spectral-matching): scale by k_{ULS}, then spectral match, then scale by $k_{Target\ (2)}$ to achieve the required pre-stressing loss.
Initial pre-stressing losses incurred from the mainshock	Range of losses from zero loss (i.e., secondary fuse not activated) up to a complete loss. The ground motions were scaled by k_{Target} to achieve various peak deformations and associated losses as shown in Appendix A.
Ratio of aftershock intensity	Range of aftershock intensities by applying scale factors of 0.5, 0.6, 0.7, 0.8, 0.9 and 1.0, after prior scaling to the same target displacement as the mainshock.

displacement targets as the mainshock (on a virgin hysteresis). Thus, if they are scaled to displacements within the primary stage (0 % loss) then the peak displacements are identical for both mainshock and aftershock, as shown in the top left figure. However, if some losses have occurred from the mainshock (secondary stage), then the lower slip forces result in amplified displacements during the aftershock. This can be seen in the top row and highlights the increased sensitivity to aftershocks.

In actual scenarios, the aftershock ratio more commonly falls below 1. This is especially the case for earthquakes that are exceptionally strong and rare, and which are intended to trigger the secondary fuse. So, the aftershock ratio of 0.75 is shown in the bottom row. In these cases, the aftershocks do not cause significant displacements compared to the mainshock. Even with 40 % loss in pre-stressing, the aftershock did not cause rupture in contrast to the top row. Hence, the vulnerability of the system to aftershocks depends on the specific combination of pre-stressing losses as well as the actual intensity of the aftershock (as measured by the aftershock ratio).

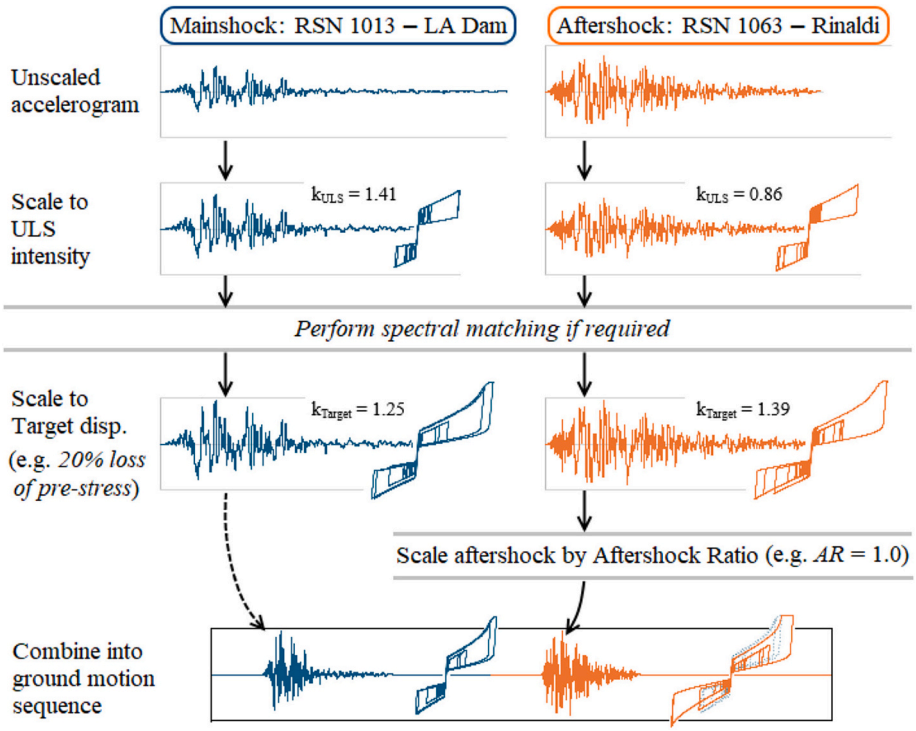

Fig. 6. Illustrating the steps to prepare ground motion sequences.

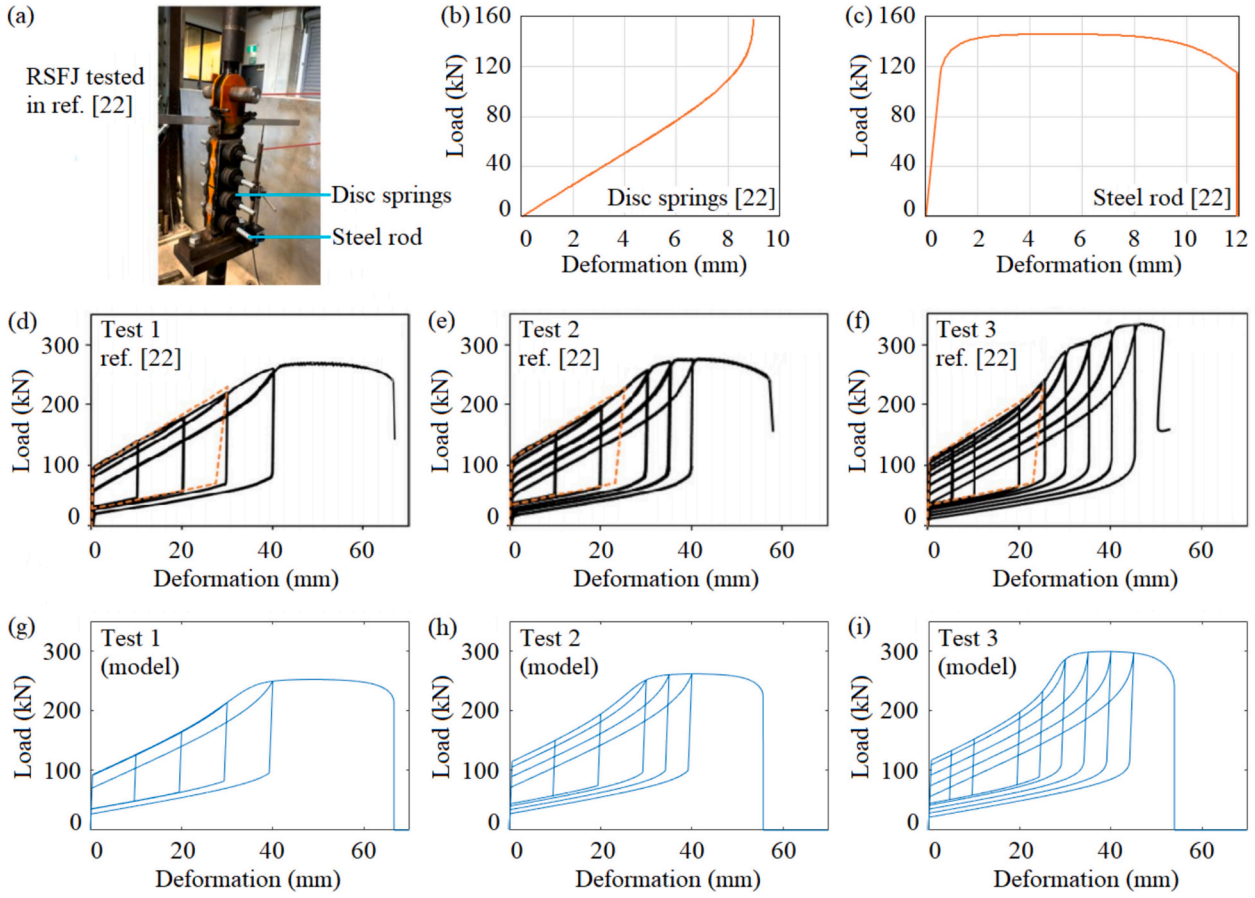

Fig. 7. Comparing the RSFJ test results from Bagheri et al. [22] against the modelled hysteresis.

Table 4
Input parameters used to model the RSFJs tested.

Test	k_i	F_{ps}	μ	θ	$SF(\Delta_{rod})$	$SF(F_{rod})$	$SF(\Delta_{disc})$	$SF(F_{disc})$
1	200	50	0.13	17.5	13/12	135/145	1	1
2	200	62	0.13	17.5	11/12	140/145	1	1
3	200	63	0.13	17.5	9.5/12	160/145	1	1

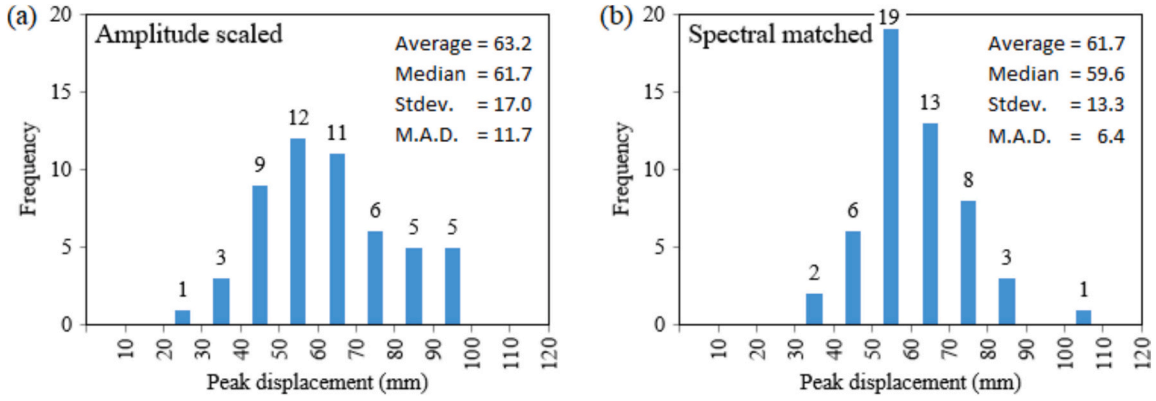

Fig. 8. Histogram of responses to design (ULS) intensity (a) scaled by k_{ULS} only (b) scaled and matched.

4.4. Responses to all ground motion sequences

Fig. 10 shows the peak displacements sustained during the ground motion sequences. For each x-value denoting the mainshock displacements, the y-value shows the corresponding aftershock displacements. A total of 15 x-coordinates are shown: 5 in the primary stage and 10 in the secondary stage according to the pre-stressing losses in Table 1. Thus, pre-stressing losses occur within the dotted lines that delineate the transition from primary-to-secondary behavior and secondary-to-rupture.

Table 5
Difference between displacement targets and responses to the ground motions scaled by $k_{ULS}k_{Target}$.

Point	1	2	3	4	5	6	7	8	9	10	11	12	13	14	15
U_{max} (mm)	15	30	45	60	76	89	96	103	109	115	122	128	134	139	143
ϵ_{amp} (%)	0.03	0.02	0.02	0.08	0.01	0.01	0.00	0.00	0.00	0.00	0.01	0.00	0.01	0.01	0.00
ϵ_{spm} (%)	0.10	0.02	0.23	0.03	0.01	0.01	0.01	0.01	0.02	0.01	0.03	0.01	0.00	0.00	0.00

Note. ϵ denotes the average error across the set of ground motions. Subscripts *amp* and *spm* denote the amplitude-scaled and spectral-matched sets of ground motions.

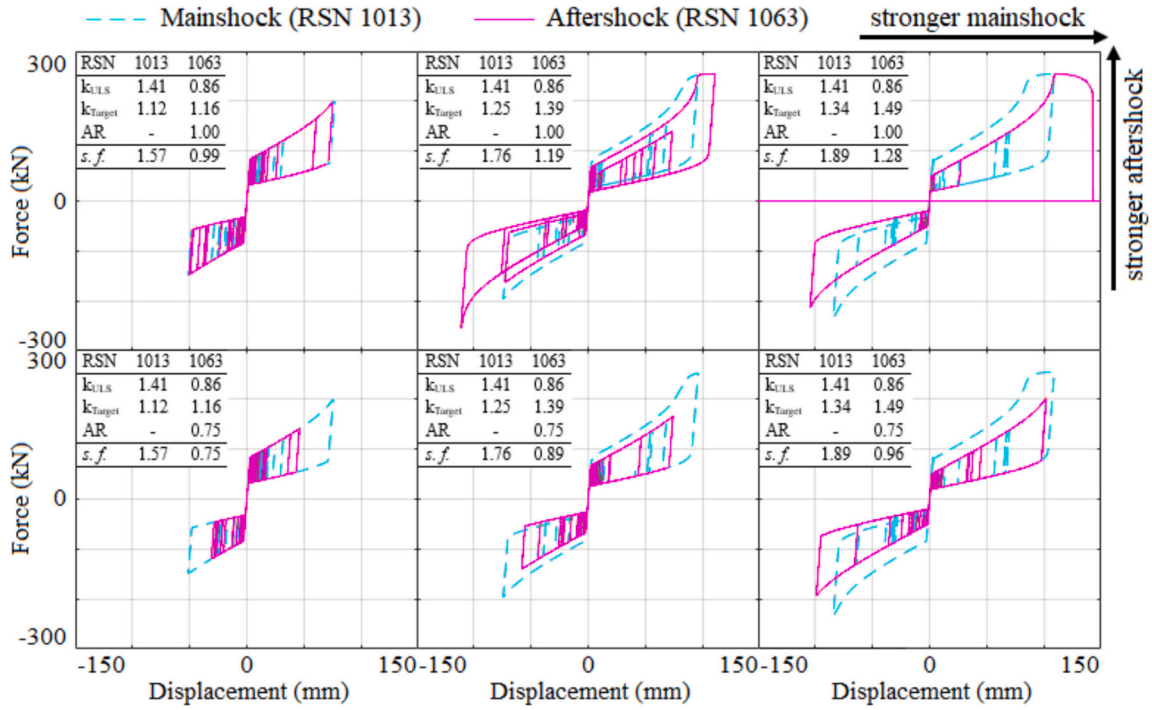

Fig. 9. Response to a ground motion sequence (Mainshock: RSN1013, Aftershock: RSN1063). Aftershock ratios of 1.0 (top) and 0.75 (bottom). Pre-stressing losses of 0 %, 20 % and 40 % (left to right).

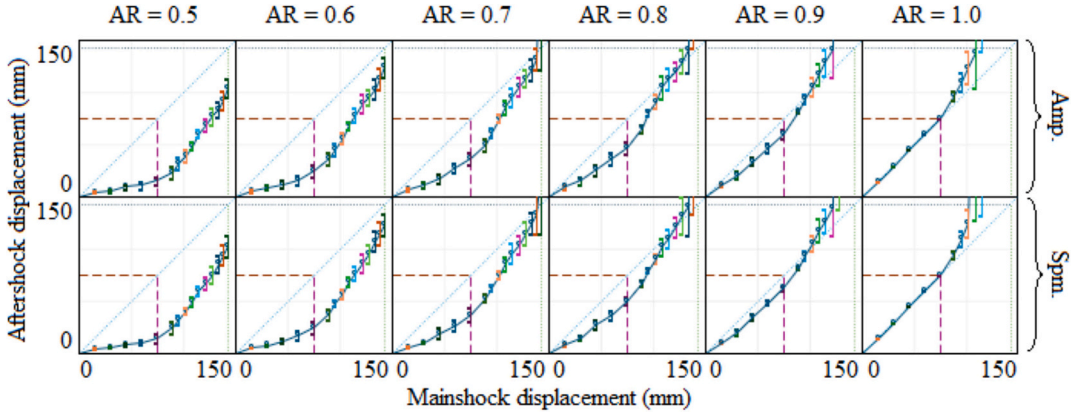

Fig. 10. Mainshock-aftershock responses in terms of medians and median absolute deviations.

Each curve represents different aftershock ratios applied. Each data point represents the median of 52^2 (= 2704) possible combinations of ground motion records. Fig. 10 shows the median values for each set and each aftershock ratio. The distributions are shown in terms of median absolute deviations (M.A.D.) because it is less susceptible to distortion from the ruptured cases consisting of very large displacements. Fig. 11 summarizes these curves and Table B1 in Appendix B shows the data for these graphs.

Data points above the x = y slope indicate that the aftershock displacements are greater than the mainshock displacements, and vice versa. As Fig. 11 shows, the aftershock displacements are not amplified if no prior losses of pre-stressing occurred during the mainshock. Hence, the curves fall on or below the x = y slope as expected for responses in the primary stage. This assumes that the aftershock is, by definition, less intense compared to the mainshock. On the other hand, if the secondary fuse has been activated during the mainshock, the response to the

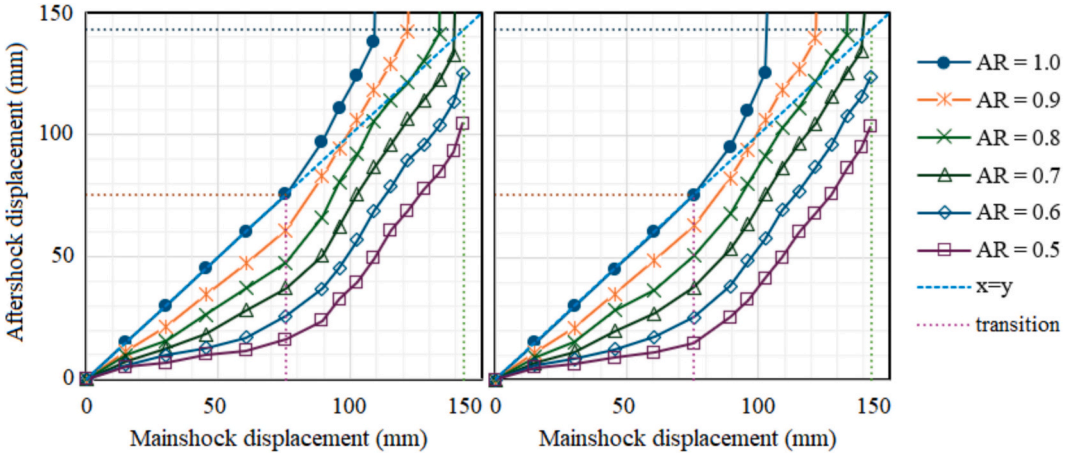

Fig. 11. Mainshock-aftershock responses for records with (a) amplitude-scaling only, (b) spectral-matching.

aftershock generally increases rapidly due to the weakened slip force. This can be seen in the upwards curves after entering the secondary stage.

For a severe aftershock ratio (AR = 1), it appears that a prior pre-stressing loss of 40 % during the mainshock weakens the system critically to cause rupture in the ensuing aftershock. At the other extreme, the aftershock displacements are all smaller than the mainshock displacements for AR = 0.6 and below, regardless of the extent of pre-stressing loss incurred during the mainshock. For AR = 0.8, the aftershock displacements are equal or smaller to the mainshock displacements, lying near the x = y slope until rupture, perhaps indicating a boundary between stable/unstable behavior.

These graphs imply that the system can withstand small-to-moderate aftershocks regardless of the severity of pre-stressing losses incurred during the prior mainshock. On the other hand, if large aftershocks are expected (0.8 < AR < 1), then the pre-stressing losses incurred from the mainshock must be kept below a maximum of 40 % (for AR = 1) or 60 % (for AR = 0.9) to avoid rupture during the aftershock.

Looking at the spectral-matched results in Fig. 11(b), the data appear to mirror the amplitude-scaled results in Fig. 11(a) except for one data point reaching rupture earlier (Point 9, AR = 1.0). However, this point was also very close to rupture in the other set of amplitude-scaled records. Another slight difference is that the curves from the spectral-matched set appear to be slightly straighter than those without matching.

One observation is that the dispersion did not differ significantly between the two sets of results in Fig. 11. In hindsight, this is likely due to the additional scaling by k_{Target} that was used to reach various pre-stressing losses. As this scaling was performed after the spectral matching process, the benefits of spectral matching were likely lost. In comparison, the graphs in Fig. 8 show that direct application of spectral-matched records without further scaling leads to smaller variations even when the system responds in the nonlinear range. A possible work-around to be explored in future studies is to spectral match the records to multiple target spectra of different intensities. This would produce multiple sets of spectral-matched records that cover the range of pre-stressing losses needed for the mainshocks.

4.5. Calibrated expressions

The combined datasets are used to fit a calibrated equation that can be applied easily. As Fig. 12(a) shows, the data points result in a good fit with a plane surface expression shown in Table 6. The equations are shown in terms of displacements, or drift percentages after normalizing by the storey height. With R^2 and adjusted R^2 values of 0.99, the goodness-of-fit is visible in Fig. 12(b) by viewing the data points from an angle along the plane. The data points appear to follow the surface closely and have relatively small perpendicular distances to the plane. The applicable limits of the fitted equation are also shown in Table 6, which are defined according to the extremities of the data points used for fitting.

Table 6
Expressions for the fitted surface in Fig. 12 on the mainshock-aftershock responses.

Type of Expression	In terms of displacements (mm)	In terms of drift (%)
Mainshock-aftershock relationships	$u_{after} = 1.59\,u_{main} + 168\,AR - 206$	$\delta_{after} = 1.59\,\delta_{main} + 5.42\,AR - 6.65$
Mainshock limits	$89\ mm \le u_{main} \le 143\ mm$	$2.9\% \le \delta_{main} \le 4.6\%$
Aftershock limits	$24\ mm \le u_{after} \le 143\ mm$	$0.8\% \le \delta_{after} \le 4.6\%$
Aftershock ratios	$0.5 \le AR \le 1.0$	$0.5 \le AR \le 1.0$

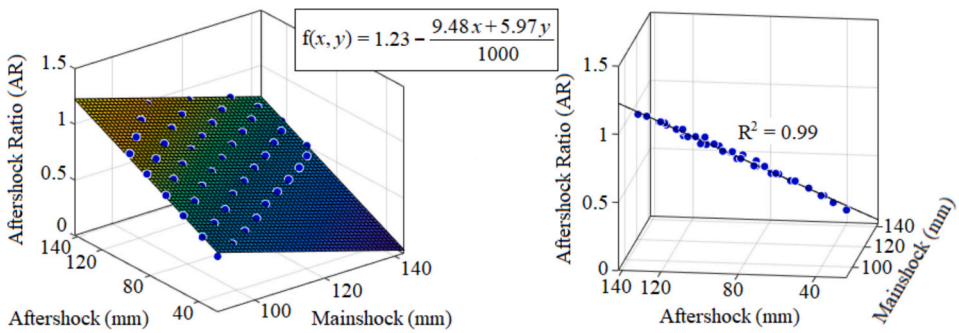

Fig. 12. (a) 3D plot of the mainshock-aftershock responses. (b) In-plane viewing angle.

The calibrated expression shows that for every unit increase in secondary displacement incurred during the mainshock, the aftershock response is expected to grow by a factor of 1.6 times (i.e., an additional 60 % greater increase in displacement). This was observed with every AR value. It indicates that any loss in pre-stressing tends to exacerbate the impacts of an aftershock, whether it is a mild or an intense aftershock. Based on the limits of the parameters examined, the response to an aftershock is therefore independently proportional to (a) the mainshock response, and (b) the intensity of the aftershock.

In a study on pinched hysteresis, Pu and Wu [31] also found a proportional relationship between the mainshock and aftershock responses. For a given aftershock ratio AR, the displacements were increasingly amplified with smaller periods. On average, the amplification factors were 0.98, 1.03, 1.08 and 1.20 for the respective periods of 2.0, 1.2, 0.8 and 0.5 s. Although the authors did not go below the period of 0.5 s, the observed trend indicates that extrapolating to a period of 0.22 s (used in this study) may land in the vicinity of 1.59 found in this study. Indeed, another study by Zhai et al. [43] also noticed an exponential increase in displacement demands for periods below 0.5 s. These observations appear to support the results obtained in the present study whereby u_{after} was found to be linearly proportional to u_{main}.

Pu and Wu [31] also observed an approximately linear relationship between the aftershock displacement response u_{after} and the aftershock ratio AR. When calibrating the responses to the term AR^b, the exponent b was close to 1 which indicates a linear relationship with AR. In Zhai et al. [43], the authors noted that the displacements start to amplify when AR approaches 0.8. Interestingly, the authors' findings appear to agree with the present study which obtained an AR of 0.8 as the transition value. As shown earlier in Fig. 11, the aftershock responses did not amplify further for curves below AR = 0.8. Instead, the aftershock displacements only exceeded the mainshock displacements at AR = 0.8 and above on average. Hence, these studies also support the present work's finding of a linear dependence between u_{after} and AR.

4.6. Cascading sequences

In longer sequences, there is a possibility of a cascading effect where the remaining pre-stress deteriorates progressively over multiple aftershocks. For instance, when an aftershock causes a pre-stressing loss, the reduced slip force increases the system's susceptibility to an even weaker aftershock. In turn, the weaker aftershock causes even further losses in pre-stressing, and the vicious cycle may continue in a cascade towards rupture.

A simple and more general way to visualize the pre-stressing losses is to plot the initial or current loss against the expected loss post-aftershock. With the information from Table 1, it is possible to convert the plot axes from displacements to pre-stressing losses as Fig. 13 shows.

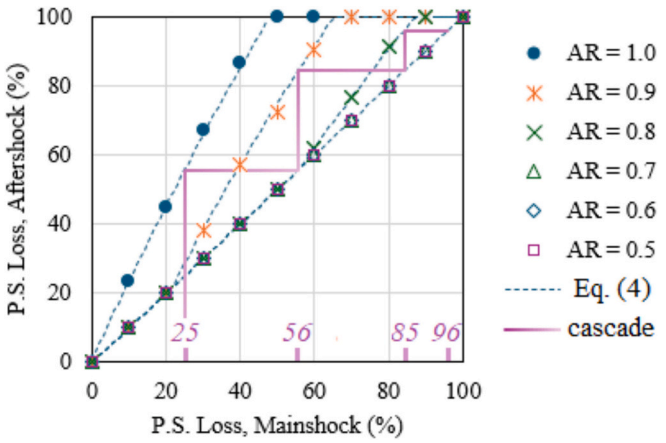

Fig. 13. Change in pre-stress loss from mainshock to aftershock.

This graphical method offers a convenient way to estimate whether the remaining pre-stress is adequate to resist future shocks, and thereby the resilience of the system against repeated earthquakes.

Fig. 13 can be used to estimate the changes in pre-stressing over multiple aftershocks. The example shown in the figure starts with an initial state of 25 % loss, which may have been caused by either a mainshock or a previous aftershock. If a first aftershock with AR = 1.0 were imposed on the system, the current loss is expected to increase to 56 %. Then, if a second aftershock with AR = 0.9 occurs, it would push the system further to 85 % loss. Finally, with a third aftershock of AR = 0.8, the expected loss in pre-stress would reach 96 %, which is close to rupture. However, if the intensity of aftershocks were below AR = 0.7 it is possible that the pre-stress does not deteriorate at all. This is noteworthy because 0.7 times the MCE-level earthquake is a very high threshold, being approximately the same intensity as the design (ULS) ground motion. It suggests a low likelihood of further losses in pre-stressing during subsequent ULS-level earthquakes.

As shown in Fig. 13, the expected loss cannot be less than the initial loss because the prior losses are irreversible. The losses are also limited to a maximum of 100 % that indicates a complete loss of pre-stressing (rupture). The fitted lines in Eqs. (4)–(5) express the percentage losses as dashed lines in Fig. 13 and they can simply be used to estimate the pre-stressing losses. On the other hand, the expressions in Table 6 are more relevant for estimating the actual aftershock displacements when they are smaller compared to the mainshock, and when the aftershock does not cause further losses in pre-stressing.

$$L_{after} = 1.635\,L_{main} + 253.1\,AR + 0.6957\,L_{main}AR - 0.005482\,L_{main}^2 - 252.2 \tag{4}$$

$$L_{main} \le L_{after} \le 100 \tag{5}$$

5. Conclusions

Under extreme loading, the Resilient Slip-Friction Joint (RSFJ) may respond beyond its primary stage and trigger the joint's secondary fuse mechanism. The secondary response is associated with irreversible yielding of steel rods, decompression of disc springs, and potentially reduced damping and self-centering capabilities. This study investigates the degradation in cyclic response (hysteresis) and whether it leads to increased vulnerability in subsequent earthquakes/aftershocks. A numerical procedure was developed to model the RSFJ's hysteresis and then used for time-history analyses of a single-degree-of-freedom (SDOF) system. It was subjected to mainshock-aftershock sequences with different amounts of initial pre-stressing losses (caused by the mainshock) and different aftershock intensities. The main findings are:

- The numerical model captured the salient features of the RSFJ's behavior throughout primary and secondary stages. It captured the (i) gradual loss of pre-stressing observed in experimental tests, (ii) highly curved hysteresis as yielding steel rods interacted with nonlinear elastic disc springs, and (iii) rupture deformation influenced by the joint properties and level of pre-stressing applied.
- The peak deformation from aftershocks appeared to vary linearly with (i) the mainshock response and associated losses in pre-stressing, and (ii) the intensity of the aftershock as denoted by the aftershock/mainshock intensity ratio (AR). This was observed for both ground motion sets, where the first set was amplitude scaled only, and the second set subjected to additional spectral matching.
- The SDOF system could survive a strong aftershock (AR > 0.8) without rupturing only if the pre-stressing losses incurred from the mainshock was limited to approximately 40–60 %. Conversely, smaller aftershocks (AR ≤ 0.6) generally produce smaller responses compared to the mainshock and do not exacerbate the initial losses in pre-stressing. This means that the SDOF system may endure multiple

aftershocks (AR $\leq$ 0.6) regardless of the pre-stressing losses incurred during the mainshock.

- The point above implies that a secondary fuse designed to activate in an MCE-level earthquake will generally be capable of resisting subsequent ULS-level earthquakes, with a low risk of further pre-stressing losses. This is because the ULS/MCE intensity ratio is typically about 0.66 in design codes.
- The findings are limited to the SDOF model examined and further work on MDOF systems is needed to understand the effects on a global structural level. While the secondary fuse offers increased deformation capacity, P-delta effects may also become more pronounced. There are also questions on whether soft-storey effects become important due to reduced slip forces, or conversely, less significant because of the RSFJ's reserve capacity (Section 2.2). Further study is recommended on the RSFJ's rupture mechanism since it may trigger redistribution of forces and alter the hierarchy of failure on a structural level.

CRediT authorship contribution statement

Nicholas Chan: Writing – original draft, Visualization, Methodology, Formal analysis, Data curation, Conceptualization. **Ashkan Hashemi:** Writing – review & editing, Supervision, Methodology, Conceptualization. **Pouyan Zarnani:** Writing – review & editing, Supervision, Methodology, Conceptualization. **Pierre Quenneville:** Writing – review & editing, Supervision, Methodology, Conceptualization.

Declaration of competing interest

The authors declare that they have no competing financial interests or personal relationships that could have inappropriately influenced the work in this paper.

Acknowledgements

The authors would like to acknowledge the financial support of the University of Auckland, New Zealand. The authors would also like to express gratitude to Setu Agarwal and Soheil Assadi for the stimulating discussions that contributed to the development of the hysteresis model.

Appendix A

Table A1
Scale factors $k_{Target\ (1)}$ for amplitude-scaled set to reach various deformations/pre-stressing losses.

RSN	1	2	3	4	5	6	7	8	9	10	11	12	13	14	15
6	0.48	0.56	0.67	0.76	0.97	0.99	1.01	1.03	1.07	1.10	1.14	1.17	1.19	1.22	1.23
135	0.47	0.70	1.02	1.18	1.28	1.41	1.47	1.54	1.60	1.65	1.69	1.72	1.75	1.76	1.78
138	0.65	0.68	0.96	1.03	1.13	1.27	1.32	1.33	1.37	1.41	1.44	1.48	1.52	1.55	1.56
161	0.48	0.67	0.79	0.89	0.99	1.08	1.12	1.16	1.20	1.24	1.26	1.28	1.30	1.32	1.33
215	0.62	0.72	0.96	1.11	1.29	1.45	1.46	1.48	1.49	1.49	1.49	1.49	1.50	1.50	1.50
266	0.56	0.66	0.77	0.94	1.00	1.11	1.20	1.28	1.39	1.42	1.44	1.47	1.50	1.51	1.52
268	0.53	0.75	0.88	0.93	0.98	1.03	1.05	1.08	1.11	1.15	1.19	1.24	1.29	1.38	1.40
316	0.61	0.77	0.78	0.92	0.95	0.99	1.03	1.19	1.22	1.25	1.29	1.33	1.35	1.37	1.38
358	0.51	0.66	0.73	0.91	1.07	1.19	1.27	1.29	1.34	1.39	1.43	1.49	1.50	1.53	1.56
366	0.43	0.68	1.05	1.20	1.29	1.40	1.45	1.49	1.53	1.55	1.58	1.60	1.62	1.63	2.09
502	0.39	0.54	0.79	0.86	0.96	1.06	1.12	1.18	1.24	1.30	1.36	1.40	1.43	1.45	1.46
504	0.53	0.70	0.80	0.85	0.95	1.03	1.07	1.13	1.18	1.19	1.20	1.21	1.21	1.22	1.23
523	0.64	0.75	0.83	0.94	1.19	1.29	1.32	1.34	1.36	1.40	1.41	1.42	1.43	1.44	1.45
569	0.68	0.74	0.85	1.09	1.14	1.20	1.23	1.26	1.29	1.32	1.34	1.37	1.40	1.42	1.43
721	0.54	0.66	0.81	1.02	1.12	1.20	1.23	1.28	1.30	1.34	1.37	1.41	1.44	1.47	1.49
729	0.55	0.72	0.85	0.98	1.14	1.26	1.33	1.39	1.46	1.48	1.49	1.51	1.52	1.53	1.53
798	0.38	0.55	0.84	0.89	0.97	1.06	1.10	1.14	1.17	1.20	1.22	1.25	1.28	1.30	1.31
802	0.58	0.91	1.22	1.26	1.31	1.38	1.42	1.47	1.50	1.51	1.57	1.59	1.60	1.61	1.62
821	0.42	0.63	0.77	0.91	1.06	1.19	1.24	1.30	1.37	1.47	1.51	1.52	1.53	1.53	1.54
827	0.64	0.69	0.74	0.82	1.00	1.06	1.12	1.21	1.30	1.37	1.43	1.46	1.49	1.52	1.54
832	0.54	0.68	0.74	0.89	1.14	1.30	1.33	1.42	1.44	1.48	1.49	1.49	1.51	1.52	1.52
930	0.60	0.66	0.74	0.83	1.02	1.10	1.20	1.31	1.40	1.49	1.65	1.67	1.67	1.68	1.69
1013	0.55	0.71	0.75	1.05	1.12	1.21	1.25	1.30	1.34	1.39	1.41	1.49	1.52	1.53	1.54
1063	0.46	0.67	0.80	0.97	1.16	1.32	1.39	1.45	1.49	1.53	1.54	1.55	1.55	1.56	1.56
1119	0.60	0.86	0.97	1.07	1.16	1.25	1.31	1.36	1.40	1.44	1.47	1.49	1.51	1.53	1.54
1119	0.49	0.53	0.91	1.03	1.16	1.34	1.39	1.45	1.49	1.54	1.57	1.60	1.63	1.66	1.67
1137	0.66	1.03	1.17	1.37	1.50	1.64	1.68	1.71	1.73	1.75	1.78	1.79	1.80	1.80	1.80
1148	0.59	0.66	0.87	1.09	1.43	1.63	1.65	1.66	1.67	1.69	1.73	1.74	1.75	1.77	1.77
1165	0.54	0.81	0.85	0.89	1.11	1.33	1.42	1.44	1.45	1.48	1.50	1.52	1.54	1.56	1.57
1268	0.54	0.66	0.72	0.78	0.81	0.94	1.03	1.11	1.19	1.26	1.32	1.35	1.39	1.41	1.42
1773	0.61	0.85	1.11	1.31	1.39	1.50	1.51	1.52	1.54	1.57	1.59	1.59	1.60	1.62	1.63
1823	0.50	0.66	0.84	0.95	1.06	1.21	1.28	1.34	1.41	1.44	1.46	1.49	1.51	1.53	1.54
2115	0.56	0.67	0.97	1.14	1.49	1.60	1.64	1.68	1.74	1.78	1.81	1.81	1.82	1.82	1.82
2958	0.68	0.88	1.02	1.04	1.11	1.18	1.18	1.19	1.21	1.23	1.27	1.31	1.35	1.38	1.41
3577	0.53	0.62	0.84	0.89	1.05	1.20	1.23	1.25	1.28	1.36	1.40	1.44	1.47	1.50	1.51
3746	0.47	0.74	0.78	0.83	0.88	0.96	1.00	1.04	1.09	1.13	1.16	1.21	1.48	1.53	1.56
3754	0.52	0.67	0.82	0.95	1.08	1.20	1.23	1.26	1.29	1.37	1.39	1.41	1.41	1.43	1.43
4113	0.57	0.66	0.73	0.81	0.90	0.99	1.04	1.08	1.12	1.15	1.17	1.20	1.22	1.23	1.24
4117	0.62	0.91	1.00	1.07	1.20	1.33	1.41	1.46	1.50	1.51	1.52	1.56	1.58	1.59	1.59
4366	0.53	0.62	0.86	0.99	1.19	1.32	1.42	1.47	1.49	1.52	1.59	1.64	1.68	1.69	1.69
4457	0.64	0.78	0.90	1.02	1.14	1.24	1.27	1.28	1.32	1.32	1.33	1.33	1.35	1.36	1.38

(continued on next page)

Table A1 (*continued*)

RSN	1	2	3	4	5	6	7	8	9	10	11	12	13	14	15
4483	0.59	0.73	0.87	1.02	1.18	1.34	1.42	1.49	1.52	1.55	1.57	1.59	1.61	1.62	1.63
4840	0.49	0.58	0.66	0.74	0.84	0.95	1.01	1.11	1.13	1.15	1.18	1.21	1.24	1.27	1.28
4855	0.79	0.88	0.89	1.04	1.07	1.25	1.33	1.40	1.41	1.42	1.42	1.43	1.43	1.43	1.44
5470	0.53	0.73	1.01	1.11	1.26	1.40	1.41	1.41	1.41	1.42	1.43	1.44	1.46	1.48	1.48
5779	0.40	0.61	0.70	0.83	0.97	1.10	1.16	1.22	1.28	1.35	1.41	1.47	1.53	1.58	1.61
5831	0.60	0.88	0.99	1.16	1.29	1.55	1.57	1.61	1.64	1.76	1.80	1.80	1.80	1.80	1.81
6014	0.57	0.79	0.92	1.03	1.37	1.74	1.79	1.83	1.84	1.85	1.87	1.90	1.90	1.91	1.91
6890	0.63	0.85	0.92	1.08	1.23	1.38	1.42	1.47	1.51	1.54	1.56	1.57	1.60	1.61	1.61
6988	0.56	0.71	0.83	0.89	1.03	1.18	1.26	1.38	1.40	1.43	1.46	1.49	1.49	1.50	1.51
8130	0.53	0.74	0.91	1.03	1.12	1.21	1.24	1.26	1.31	1.34	1.37	1.39	1.41	1.43	1.43
8134	0.58	0.70	0.85	1.03	1.21	1.43	1.44	1.46	1.46	1.47	1.48	1.49	1.50	1.50	1.51

Table A2
Scale factors $k_{Target\ (2)}$ for spectral-matched set to reach various deformations/pre-stressing losses.

RSN	1	2	3	4	5	6	7	8	9	10	11	12	13	14	15
6	0.53	0.72	0.88	1.16	1.31	1.45	1.54	1.54	1.58	1.62	1.65	1.68	1.68	1.68	1.68
135	0.61	0.72	0.81	0.92	1.06	1.19	1.24	1.30	1.35	1.41	1.46	1.51	1.55	1.59	1.61
138	0.59	0.72	0.82	0.99	1.14	1.22	1.26	1.30	1.33	1.38	1.41	1.48	1.52	1.58	1.60
161	0.45	0.60	0.71	0.83	0.96	1.12	1.17	1.20	1.23	1.27	1.30	1.32	1.34	1.37	1.38
215	0.58	0.68	0.98	1.16	1.40	1.61	1.67	1.69	1.70	1.70	1.71	1.71	1.71	1.72	1.72
266	0.59	0.69	0.88	1.13	1.24	1.43	1.43	1.48	1.48	1.48	1.49	1.49	1.49	1.52	1.53
268	0.60	0.76	0.92	1.14	1.16	1.20	1.24	1.32	1.34	1.37	1.40	1.46	1.49	1.51	1.53
316	0.63	0.78	0.90	0.95	1.12	1.23	1.25	1.40	1.46	1.52	1.58	1.62	1.66	1.69	1.71
358	0.54	0.74	0.99	1.05	1.28	1.40	1.50	1.54	1.66	1.67	1.69	1.70	1.71	1.71	1.71
366	0.65	0.70	0.89	1.04	1.20	1.35	1.41	1.47	1.52	1.54	1.56	1.58	1.60	1.63	1.64
502	0.58	0.75	0.83	0.90	1.00	1.11	1.18	1.25	1.33	1.36	1.38	1.40	1.42	1.43	1.43
504	0.61	0.80	0.90	1.03	1.15	1.38	1.42	1.45	1.47	1.48	1.48	1.48	1.48	1.48	1.49
523	0.58	0.70	0.82	1.00	1.22	1.33	1.34	1.38	1.39	1.39	1.39	1.40	1.42	1.45	1.51
569	0.60	0.74	0.81	0.86	0.94	1.05	1.12	1.19	1.42	1.48	1.51	1.53	1.56	1.58	1.60
721	0.48	0.66	0.95	1.23	1.36	1.42	1.49	1.57	1.61	1.65	1.71	1.73	1.73	1.73	1.73
729	0.61	0.63	0.90	0.96	1.05	1.18	1.39	1.44	1.49	1.54	1.57	1.59	1.60	1.61	1.61
798	0.51	0.68	0.80	0.90	1.01	1.13	1.19	1.25	1.30	1.33	1.37	1.40	1.42	1.45	1.46
802	0.59	0.79	0.92	0.98	1.16	1.21	1.30	1.33	1.34	1.36	1.38	1.40	1.41	1.42	1.42
821	0.52	0.70	0.88	1.03	1.16	1.29	1.32	1.36	1.42	1.44	1.45	1.46	1.46	1.47	1.47
827	0.57	0.66	0.74	0.84	0.97	1.07	1.13	1.19	1.26	1.31	1.36	1.37	1.38	1.39	1.41
832	0.63	0.69	0.80	0.92	1.09	1.22	1.30	1.37	1.44	1.51	1.56	1.57	1.57	1.58	1.58
930	0.57	0.72	0.88	1.05	1.21	1.39	1.43	1.46	1.49	1.50	1.51	1.52	1.52	1.53	1.53
1013	0.60	0.71	0.79	0.89	1.01	1.13	1.19	1.24	1.29	1.34	1.39	1.43	1.46	1.49	1.51
1063	0.54	0.59	0.87	1.05	1.18	1.29	1.35	1.40	1.45	1.47	1.49	1.51	1.52	1.53	1.54
1119	0.50	0.68	0.83	0.98	1.12	1.24	1.28	1.32	1.34	1.37	1.40	1.42	1.44	1.46	1.47
1119	0.58	0.79	1.00	1.05	1.11	1.20	1.25	1.30	1.35	1.39	1.43	1.48	1.53	1.57	1.60
1137	0.59	0.74	0.89	1.00	1.24	1.32	1.38	1.43	1.48	1.54	1.59	1.61	1.64	1.66	1.67
1148	0.56	0.63	0.71	0.81	0.87	0.99	1.06	1.12	1.18	1.24	1.35	1.49	1.57	1.63	1.66
1165	0.68	0.79	0.84	1.01	1.18	1.35	1.41	1.44	1.53	1.55	1.57	1.58	1.61	1.61	1.62
1268	0.62	0.74	0.94	1.09	1.17	1.31	1.37	1.40	1.45	1.46	1.48	1.49	1.50	1.51	1.52
1773	0.58	0.84	0.93	1.04	1.20	1.39	1.44	1.58	1.60	1.64	1.67	1.71	1.77	1.78	1.79
1823	0.48	0.63	0.87	1.09	1.29	1.43	1.47	1.51	1.53	1.54	1.54	1.56	1.59	1.60	1.61
2115	0.63	0.73	0.99	1.07	1.25	1.31	1.34	1.36	1.38	1.39	1.39	1.39	1.40	1.42	1.43
2958	0.57	0.73	0.97	1.02	1.04	1.06	1.08	1.12	1.25	1.29	1.34	1.35	1.36	1.36	1.37
3577	0.52	0.69	0.80	0.89	0.99	1.09	1.15	1.21	1.27	1.31	1.35	1.38	1.41	1.44	1.45
3746	0.57	0.77	0.94	1.00	1.07	1.18	1.22	1.26	1.30	1.32	1.34	1.36	1.37	1.39	1.40
3754	0.61	0.76	1.02	1.09	1.23	1.39	1.47	1.53	1.58	1.62	1.66	1.69	1.72	1.74	1.75
4113	0.54	0.65	0.75	0.85	0.96	1.06	1.12	1.18	1.22	1.25	1.28	1.30	1.33	1.36	1.39
4117	0.50	0.62	0.82	1.01	1.30	1.42	1.47	1.53	1.58	1.63	1.68	1.71	1.74	1.75	1.76
4366	0.67	0.91	0.98	1.12	1.40	1.46	1.50	1.56	1.57	1.58	1.60	1.62	1.63	1.65	1.67
4457	0.53	0.72	0.88	0.98	1.08	1.20	1.27	1.33	1.38	1.43	1.46	1.47	1.48	1.49	1.49
4483	0.50	0.63	0.73	0.84	0.97	1.11	1.18	1.24	1.28	1.31	1.34	1.36	1.38	1.39	1.40
4840	0.45	0.53	0.60	0.68	0.77	0.87	0.93	0.98	1.04	1.09	1.13	1.17	1.20	1.22	1.24
4855	0.64	0.81	0.89	1.08	1.28	1.57	1.69	1.72	1.73	1.74	1.74	1.75	1.75	1.75	1.76
5470	0.51	0.80	0.87	1.08	1.22	1.36	1.38	1.40	1.43	1.45	1.47	1.48	1.50	1.51	1.51
5779	0.52	0.61	0.78	0.90	1.01	1.11	1.17	1.23	1.28	1.33	1.38	1.42	1.45	1.48	1.50
5831	0.55	0.72	0.95	1.06	1.21	1.40	1.43	1.43	1.45	1.48	1.51	1.54	1.55	1.56	1.57
6014	0.59	0.82	1.03	1.03	1.06	1.20	1.43	1.54	1.57	1.60	1.63	1.67	1.71	1.72	1.78
6890	0.60	0.85	1.03	1.17	1.25	1.33	1.37	1.40	1.45	1.45	1.52	1.52	1.52	1.53	1.56
6988	0.57	0.72	0.88	1.01	1.17	1.34	1.44	1.51	1.57	1.65	1.67	1.68	1.69	1.69	1.70
8130	0.63	0.84	0.93	1.06	1.33	1.54	1.66	1.71	1.72	1.72	1.73	1.74	1.74	1.75	1.75
8134	0.62	0.74	1.03	1.26	1.46	1.54	1.59	1.61	1.63	1.64	1.65	1.66	1.67	1.67	1.68

Appendix B

Table B1
Aftershock peak displacements (mm) after being subjected to various mainshock intensities.

Set	AR	1	2	3	4	5	6	7	8	9	10	11	12	13	14	15
Median	0.5	5	7	10	12	16	24	33	40	50	61	69	78	84	93	105
(Amp. set)	0.6	6	10	13	17	26	37	46	57	69	79	90	96	104	113	125
	0.7	7	13	18	28	37	50	63	76	87	96	106	114	122	133	*rup.*
	0.8	10	16	26	37	48	66	81	92	106	114	121	130	141	*rup.*	*rup.*
	0.9	12	22	35	47	61	83	95	106	118	129	142	*rup.*	*rup.*	*rup.*	*rup.*
	1.0	15	30	45	60	75	97	111	124	138	*rup.*	*rup.*	*rup.*	*rup.*	*rup.*	*rup.*
M.A.D.	0.5	0.9	1.6	1.9	3.2	3.9	5.9	6.0	5.6	4.3	3.4	5.8	7.9	7.7	8.8	8.6
(Amp. set)	0.6	1.2	2.1	3.1	4.5	6.1	6.4	5.9	4.9	3.6	6.6	8.7	7.0	9.4	10.1	9.6
	0.7	1.4	2.8	4.5	4.3	6.2	6.4	4.6	3.5	6.8	8.5	8.9	8.0	10.7	10.8	–
	0.8	1.6	3.1	4.8	5.3	5.5	3.9	2.9	6.2	10.5	10.4	8.6	10.9	21.1	–	–
	0.9	1.4	3.3	3.6	3.7	4.5	1.2	4.7	8.3	10.6	11.9	27.5	–	–	–	–
	1.0	0.0	0.0	0.0	0.0	0.0	4.4	8.9	15.6	33.8	–	–	–	–	–	–
Median	0.5	5	6	9	11	15	26	33	42	50	60	68	76	86	95	103
(Spm. set)	0.6	6	8	12	18	26	38	49	58	69	77	87	96	108	116	124
	0.7	7	11	20	27	38	54	64	76	87	96	105	116	125	134	*rup.*
	0.8	9	15	28	37	51	68	80	91	103	111	122	132	141	*rup.*	*rup.*
	0.9	11	21	35	49	63	82	94	106	119	127	140	*rup.*	*rup.*	*rup.*	*rup.*
	1.0	15	30	45	60	75	95	110	125	*rup.*	*rup.*	*rup.*	*rup.*	*rup.*	*rup.*	*rup.*
M.A.D.	0.5	0.4	0.6	1.7	1.9	3.7	5.7	4.6	2.9	4.1	4.0	6.3	8.0	7.9	9.9	9.9
(Spm. set)	0.6	0.5	1.3	2.1	4.7	6.0	5.2	3.1	3.8	4.0	6.7	9.2	9.0	9.8	10.8	10.7
	0.7	0.8	1.4	5.0	4.8	6.2	3.8	2.7	3.4	7.0	9.4	9.2	10.6	10.5	19.7	–
	0.8	1.1	2.5	4.6	4.2	4.1	2.4	2.3	5.0	8.3	8.8	9.3	17.2	26.9	–	–
	0.9	1.1	2.7	2.9	2.3	2.7	1.4	4.2	7.2	11.5	10.8	26.3	–	–	–	–
	1.0	0.0	0.0	0.0	0.0	0.0	3.6	7.3	13.5	–	–	–	–	–	–	–

Note: *rup.* Indicates that the median displacement exceeds the rupture displacement.

Data availability

Data will be made available on request.

References

[1] O. Filippova, K. Elwood, T. Collins, Re-emerging from the rubble: what is delaying regeneration of christchurch CBD?, in: NZSEE 2021 Conf., 2021. Paper 187.

[2] A. Kaiser, C. Holden, J. Beavan, D. Beetham, R. Benites, A. Celentano, D. Collett, J. Cousins, M. Cubrinovski, G. Dellow, P. Denys, E. Ficlding, B. Fry, M. Gerstenberger, R. Langridge, C. Massey, M. Motagh, N. Pondard, G. McVerry, J. Ristau, M. Stirling, J. Thomas, S.R. Uma, J. Zhao, The Mw 6.2 Christchurch earthquake of February 2011: Preliminary report, New Zeal. J. Geol. Geophys. 55 (2012) 67–90, https://doi.org/10.1080/00288306.2011.641182.

[3] M. Papathoma-Köhle, Letter to the editor: latest earthquakes in Santorini reveal the need for a multi-hazard and multi-vulnerability approach to disaster risk reduction, Nat. Hazards (2025), https://doi.org/10.1007/s11069-025-07246-8.

[4] K. Sirorattanakul, J.D. Wilding, M. Acosta, Y. Li, Z.E. Ross, S.J. Bourne, J. van Elk, J.-P. Avouac, Bursts of fast propagating swarms of induced earthquakes at the Groningen gas field, Seismol. Res. Lett. 96 (2024), https://doi.org/10.1785/0220240107.

[5] J. Colbert, K. Sila-Nowicka, J. Yao, Driving forces of population change following the Canterbury earthquake sequence, New Zealand: a multiscale geographically weighted regression approach, Popul. Space Place 28 (2022), https://doi.org/10.1002/psp.2583.

[6] G. Cremen, E. Seville, J.W. Baker, Modeling post-earthquake business recovery time: an analytical framework, Int. J. Disaster Risk Reduct. 42 (2020) 101328, https://doi.org/10.1016/j.ijdrr.2019.101328.

[7] M. Bruneau, G.A. MacRae, Reconstructing Christchurch: A Seismic Shift in Building Structural Systems, The Quake Centre, University of Canterbury, 2017.

[8] S.J. Hogg, D.A. Elliott, T. Maley, S. Broglio, T. Holden, S. Giorgini, Case studies on the practical application of resilient building technologies applied in New Zealand, Struct. Eng. Int. 30 (2020) 232–241, https://doi.org/10.1080/10168664.2020.1714531.

[9] F. Freddi, C. Galasso, G. Cremen, A. Dall'Asta, L. Di Sarno, A. Giaralis, F. Gutiérrez-Urzúa, C. Málaga-Chuquitaype, S.A. Mitoulis, C. Petrone, A. Sextos, L. Sousa, K. Tarbali, E. Tubaldi, J. Wardman, G. Woo, Innovations in earthquake risk reduction for resilience: recent advances and challenges, Int. J. Disaster Risk Reduct. 60 (2021), https://doi.org/10.1016/j.ijdrr.2021.102267.

[10] N. Chan, A. Hashemi, P. Zarnani, P. Quenneville, Pinching-free connector in a self-centering braced frame, J. Struct. Eng. 149 (2023) 04023083, https://doi.org/10.1061/JSENDH.STENG-12211.

[11] J. Erochko, C. Christopoulos, R. Tremblay, Design and testing of an enhanced-elongation telescoping self-centering energy-dissipative brace, J. Struct. Eng. 141 (2015) 04014163, https://doi.org/10.1061/(ASCE)ST.1943-541X.0001109.

[12] W. Wang, C. Fang, J. Liu, Self-centering beam-to-column connections with combined Superelastic SMA bolts and steel angles, J. Struct. Eng. 143 (2017) 04016175, https://doi.org/10.1061/(asce)st.1943-541x.0001675.

[13] P. Zarnani, A. Valadbeigi, P. Quenneville, Resilient slip friction (RSF) joint: A novel connection system for seismic damage avoidance design of timber structures, in: World Conf. Timber Eng., TU Wien, Vienna, Austria, 2016, pp. 4752–4760.

[14] A. Hashemi, P. Zarnani, R. Masoudnia, P. Quenneville, Experimental testing of rocking cross-laminated timber walls with resilient slip friction joints, J. Struct. Eng. 144 (2018) 04017180, https://doi.org/10.1061/(ASCE)ST.1943-541X.0001931.

[15] H. Bagheri, A. Hashemi, S.M.M. Yousef-Beik, P. Zarnani, P. Quenneville, New self-centering tension-only brace using resilient slip-friction joint: experimental tests and numerical analysis, J. Struct. Eng. 146 (2020) 04020219, https://doi.org/10.1061/(asce)st.1943-541x.0002789.

[16] S.M.M. Yousef-beik, S. Veismoradi, P. Zarnani, P. Quenneville, Design and testing of a self-centering friction damper-brace for compression ultimate limit state: inelastic buckling, Structures 62 (2024) 106166, https://doi.org/10.1016/j.istruc.2024.106166.

[17] S. Shabankareh, Seismic Damage Avoidance Design of Moment Resisting Frames Using a New Self-Centring Friction Connection System, Auckland University of Technology, 2020.

[18] S. Assadi, A. Hashemi, C. Clifton, P. Quenneville, G. MacRae, H. Bagheri, J. Liang-Jiu, Z. Yan, P. Zarnani, Shake-table testing of the resilient slip friction joints, in: Proc. NZSEE 2024 Annu. Conf., New Zealand Society for Earthquake Engineering, Wellington, New Zealand, 2024.

[19] P. Zhang, M.C.H. Yam, K. Ke, Y. Song, M. Zhu, Experimental study of a self-centering damper with multistage energy-dissipation mechanism, J. Struct. Eng. 150 (2024) 04024166, https://doi.org/10.1061/jsendh.steng-13665.

[20] J. Wang, J. Han, J. Xu, Development of an innovative ring spring-based self-centering friction damper, J. Constr. Steel Res. 227 (2025) 109363, https://doi.org/10.1016/j.jcsr.2025.109363.

[21] Y. Wang, Z. Zhou, L. Zhang, K. Zhao, Hysteretic behavior of dual-self-centering variable friction damper braces with low Pretensioned force, J. Earthq. Eng. 27 (2023) 142–161, https://doi.org/10.1080/13632469.2021.1997840.

[22] H. Bagheri, A. Hashemi, P. Zarnani, P. Quenneville, The resilient slip friction joint tension-only brace beyond its ultimate level, J. Constr. Steel Res. 172 (2020) 106225, https://doi.org/10.1016/j.jcsr.2020.106225.

[23] F. Mohammadi Darani, P. Zarnani, S. Veismoradi, S.M.M. Yousef-beik, A. Hashemi, P. Quenneville, Resilient slip friction joint performance: component analysis, spring model and anti-locking mechanism, Structures 33 (2021) 3897–3911, https://doi.org/10.1016/j.istruc.2021.06.075.

[24] E. Nastri, M. Latour, O. Pecorari, V. Piluso, Experimental lap-shear tests on friction dampers with single and double slotted holes, Eng. Struct. 308 (2024) 117968, https://doi.org/10.1016/j.engstruct.2024.117968.

[25] N. Priestley, Overview of PRESSS research program, PCI J. 36 (1991) 50–57, https://doi.org/10.15554/pcij.07011991.50.57.

[26] Y.L. Mo, W.L. Hwang, The effect of prestress losses on the seismic response of prestressed concrete frames, Comput. Struct. 59 (1996) 1013–1020.

[27] G. Granello, A. Palermo, S. Pampanin, T. Smith, F. Sarti, The implications of post-tensioning losses on the seismic response of pres-lam frames, Bull. N. Z. Soc. Earthq. Eng. 51 (2018) 57–69, https://doi.org/10.5459/bnzsee.51.2.57-69.
[28] T. Lou, W. Wang, Post-fire seismic behaviour of a self-centring connection with buckling-restrained plates and pre-stressed bars, Eng. Struct. 269 (2022) 114814, https://doi.org/10.1016/j.engstruct.2022.114814.
[29] N. Chan, A. Hashemi, P. Zarnani, P. Quenneville, Pinching-free connector for timber structures, J. Struct. Eng. 147 (2021) 04021036, https://doi.org/10.1061/(ASCE)ST.1943-541X.0002982.
[30] R.A. Medina, H. Krawinkler, Influence of hysteretic behavior on the nonlinear response of frame structures, in: Proc. 13th World Conf. Earthq. Eng., Vancouver, BC, 2004.
[31] W. Pu, M. Wu, Ductility demands and residual displacements of pinching hysteretic timber structures subjected to seismic sequences, Soil Dyn. Earthq. Eng. 114 (2018) 392–403, https://doi.org/10.1016/j.soildyn.2018.07.037.
[32] N. Chan, A. Hashemi, S. Agarwal, P. Zarnani, P. Quenneville, Experimental testing of a rocking cross-laminated Timber Wall with pinching-free connectors, J. Struct. Eng. 149 (2023) 1–18, https://doi.org/10.1061/jsendh.steng-12389.
[33] Tectonus, Introduction & Design Guide, 2024.
[34] Standards New Zealand, Structural design actions. Part 5: Earthquake actions – New Zealand (incorporating Amendment No. 1). NZS 1170.5:2004., New Zealand, 2016.
[35] N. Chan, A. Hashemi, P. Zarnani, P. Quenneville, Damping-ductility relationships for flag-shaped hysteresis, J. Struct. Eng. 147 (2021) 04021093, https://doi.org/10.1061/(asce)st.1943-541x.0003055.
[36] A.K. Chopra, Dynamics of Structures: Theory and Applications to Earthquake Engineering, Fourth edition, Prentice Hall, Englewood Cliffs, NJ, 2011, https://doi.org/10.1017/CBO9781107415324.004.
[37] J.L. Humar, Dynamics of Structures, Third edition, CRC Press, London, 2012.
[38] R.P. Brent, An algorithm with guaranteed convergence for finding a zero of a function, Comput. J. 14 (1971) 422–425, https://doi.org/10.1093/comjnl/14.4.422.
[39] T.D. Ancheta, R.B. Darragh, J.P. Stewart, E. Seyhan, W.J. Silva, B.S.J. Chiou, K. E. Wooddell, R.W. Graves, A.R. Kottke, D.M. Boore, T. Kishida, J.L. Donahue, NGA-West2 database, Earthquake Spectra 30 (2014) 989–1005, https://doi.org/10.1193/070913EQS197M.
[40] P. Bazzurro, N. Luco, Do scaled and spectrum-matched near-source records produce biased nonlinear structural responses?, in: Proc. 8th US Natl. Conf. Earthq. Eng., 2006.
[41] L. Al Atik, N. Abrahamson, An improved method for nonstationary spectral matching, Earthquake Spectra 26 (2010) 601–617, https://doi.org/10.1193/1.3459159.
[42] R.M. Pirooz, S. Habashi, A. Massumi, Required time gap between mainshock and aftershock for dynamic analysis of structures, Bull. Earthq. Eng. 19 (2021) 2643–2670, https://doi.org/10.1007/s10518-021-01087-z.
[43] C.H. Zhai, W.P. Wen, S. Li, Z.Q. Chen, Z. Chang, L.L. Xie, The damage investigation of inelastic SDOF structure under the mainshock-aftershock sequence-type ground motions, Soil Dyn. Earthq. Eng. 59 (2014) 30–41, https://doi.org/10.1016/j.soildyn.2014.01.003.